Universität Ulm
Fakultät für Naturwissenschaften
Energy Science and Technology

Deutsches Zentrum für Lust-und Raumfahrt e. V. (DLR)
Institut für Technische Thermodynamik
Elektrochemische Energietechnik (ECE)

Master Thesis

from
Feihong Song

Development and characterization of nanostructured oxygen electrocatalysts for anode of PEM electrolyzer

Prüfer: Prof. Dr. Werner Tillmetz, Prof. Dr. Timo Jacob
Betreuer: Prof. Dr. K. Andreas Friedrich
Li Wang

Stuttgart, 20.09.2016

DECLARATION

I here declare that the thesis entitled, “Development and characterization of nanostructured oxygen electrocatalysts for anode of PEM electrolyzer”, was written and originated entirely by me. Any information and ideas derived from published work of others are acknowledged in the test and references are given in the Bibliography.

I further declare that this work has not been submitted to other institutes besides Ulm University and Deutsches Zentrum für Luft- und Raumfahrt e. V. (DLR).

Stuttgart, 09.2016

(Feihong Song)

ACKNOWLEDGEMENT

I would first likely to thank the whole DLR staff of Stuttgart and Prof. Dr. K. Andreas Friedrich, who gave me the opportunity to write my thesis in this brilliant institute and enlighten me the first glance of research.

Then I would also like to express my gratitude to Prof. Dr. Tillmetz and Prof. Dr. Timo to be my internal supervisors and allow me to do this thesis outside Ulm University.

Also, I would like to express my sincere heartfelt thanks to my supervisor Li Wang who gives me his constant help, read my thesis with great care and offered me invaluable advice and informative suggestions.

Meanwhile, I would like to thank all the staff in TT-ECE apartment, especially the water electrolysis team managed by Dr. Fabian Burggraf and Dr. Aldo Gago. Special thanks to Ina Plock for the SEM and EDX characterization and Seybold Ingeborg for her technical support.

Last but not least, I would like to express my thanks to my parent for their valuable encouragement and spiritual support during my study. This accomplishment would not have been possible without them.

Feihong Song

Stuttgart, 09.2016

ABSTRACT

This thesis mainly focuses on developing highly active and stable anode catalysts for polymer electrolyte membrane electrolyzer by the means of using one aerogel substrate material and optimizing thermal treatment protocols. Here we focus on the iridium based catalyst since it is still the best feasible oxygen evolution reaction (OER) catalysts in acid medium so far. In this thesis, two strategies were applied to achieve this goal: i) nanosized iridium particles were dispersed on porous aerogel antimony- or niobium-doped tin dioxide (ATO or NTO); ii) different thermal treatment protocols were used for bimetallic IrRu.

Catalysts were prepared using wet chemical synthesis method by reducing $IrCl_3$ or $RuCl_3$ in anhydrous ethanol. By adding aerogel support and introducing vanadium, the mass activity and stability of the catalyst were improved. Electrochemical characterization, such as cyclic voltammogram (CV), chronopotentiometry, chronoamperometry and electrochemical impedance spectroscopy (EIS) were used for evaluating its electrochemical performance; SEM and EDX were carried out to analyze the morphologies and elements distribution of the catalysts. In addition, copper under potential deposition (Cu-UPD) on supported iridium catalysts was performed to determine the number of surface iridium atoms available for electrochemical reaction. Furthermore, bimetallic IrRu catalyst was thermally treated using various thermal treatment protocols and evaluated electrochemically by cyclic voltammogram.

The results reveal that the aerogel supported catalysts possess superior electrochemial properties, either activity or stability, comparing to state of the art unsupported iridium catalyst. And also the thermally treated iridium-ruthenium oxide exhibits different OER performances when they were applied under different thermal treatment temperatures.

Keywords: OER catalyst Iridium Aerogel support Activity Stability

ABBREVIATION

Abbreviations	Explanations
ATO	Antimony-doped tin dioxide
CTAB	Cetyltrimethylammonium bromide
CV	Cyclic voltammetry
EC	Electrochemical oxidation
EIS	Electrochemical impedance spectroscopy
EDX	Energy-dispersive X-ray
GC	Glassy carbon
GDL	Gas diffusion layer
MEA	Membrane electrode assembly
NTO	Niobium-doped tin dioxide
OER	Oxygen evolution reaction
PEMWE	Proton exchange membrane water electrolyzer
RDE	Rotating disk electrode
RHE	Reversible hydrogen electrode
SEM	Scanning electron microscopy
UPD,OPD	Under-potential deposition, Over-potential deposition

Contents

1. Introduction

Nowadays, the increasing demands of energy production and environmental issues have speeded up the energy transition from traditional fossil-oriented energy to renewable energy. Hydrogen as an energy vector can be used to overcome the intermittency of the renewable energy source, such as wind energy and solar energy. Besides, hydrogen has many advantages compared with traditional liquid and solid form of energy: it is environment friendly and renewable, it can be widely used in the fields where fossil fuels are used, itself has a higher efficiency than other fuels.[1] In order to perform the energy transfer as well as to meet the global growing demand of energy while decreasing the environmental pollution, a carbon-free power of at least 10TW (terawatt) should be accomplished by the middle of 21st century.[2]. Since hydrogen is not naturally present as molecular form, an effective hydrogen production method needs to be developed. State of the art carbon-free hydrogen production methods are steam reforming and alkaline water electrolysis. However, steam reforming method of fossil fuels produces low purity hydrogen with a large amount of carbon monoxide. Other than that, steam reforming still depends on scarce fossil fuels. Alkaline water electrolysis is a well-developed technology for producing hydrogen, but alkaline water electrolysis shows slower response time, safety and gas purity issue which push the research trend to proton exchange membrane (PEM) water electrolysis in acidic media.[3,4]

Water electrolysis is one of the carbon free technologies for hydrogen production. However, over the decades, the increasing price of electricity has obstructed the development of electrolytic hydrogen production.[5] This situation is about to change due to rapid growth of renewable energy sources such as solar cell and wind in recent years.[6] At low temperature, water electrolysis can take place among various environments both in alkaline or acid solutions. In the case of acid electrolyzer, it has advantages with respect to its high current density, higher efficiency, longer lifetime, lower maintenance cost, higher operating pressure,etc.[3,4] .

The key problem for PEM electrolyzer is to find a proper oxygen evolution reaction (OER) catalyst since anode reaction is much slower than cathode reaction.[3] State of the art OER catalyst is unsupported iridium catalyst. However, iridium is extremely expensive and one of the rarest element on earth with an production and consumption value of only 4 to 5 tons per year.[7,8,9]

This paper will focus on reducing the iridium loading while maintain a high performance of the PEM electrolyzer by several proposed approaches such as reducing the particle size in order to increase the electrochemical surface area, using different electro-ceramic supports, or changing the surface structure.[10,11,12] Previous work at German Aerospace center has developed a method that produces a highly active nanostructured iridium catalyst for anode reaction of proton exchange membrane (PEM) electrolysis, which will be used in this thesis.[7]

2. Theory

2.1 PEM water electrolysis

Water electrolysis can trace its history to the first industrial revolution, in year 1800, when Nicholson and Carlisle discovered electrolytical water decomposing. For the following years, solid polymer electrolyte system (SPE) and alkaline systems were manufactured and in operation.[13] The history ends up with the development of proton exchange membranes (PEM) by DuPont as well as other manufacturers.[13] A proton exchange membrane is a polymeric membrane generally formed by ionomer and used to conduct protons while being an insulator and reactant barrier. It is also acting as a binder to provide a three dimensional stable structure. Owing to the great innovation of proton exchange membrane, as mentioned in the introduction part, the PEM electrolysis has several advantages compare to the state of art alkaline electrolysis.

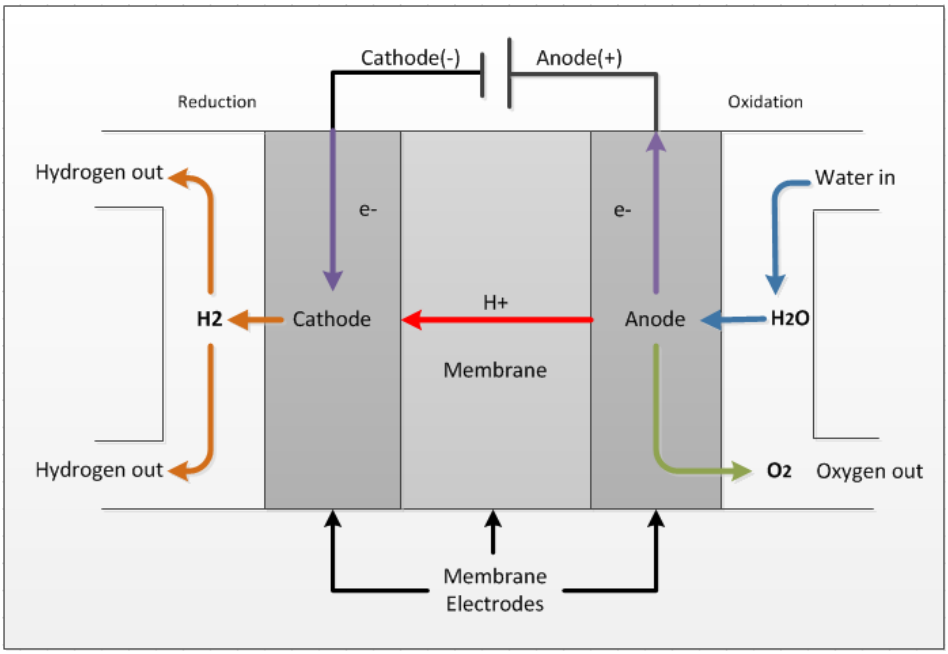

Figure 2-1 Schematic sketch of PEM electrolyzer cell

The electrolyzer cell is composed of typically three components: the membrane electrode assembly (MEA), the current collectors and the separator plates. The current collector used in Fuel Cell applications, normally carbon paper, can't be used at the anode side of PEM water electrolysis. That is due to the high potential (usually >2.0V) and acidic environment on the anode side that will oxidize carbon into carbon dioxide, thus loss its function completely and causing other problem such as cell expansion.[3] Hydrogen embrittlement is another problem in

PEM water electrolysis, which can be solved using gold plated material but in the same time resulting in an increase in capital cost.[14]

In a PEM electrolyzer, water is supplied in the anode side of the cell, where the oxygen evolution reaction takes place. Water diffuses through the current collector to the catalyst layer, where it decomposed into protons, electrons and release oxygen. The oxygen then back diffuses through the anode current collector and separator plate to get out of the cell. The electrons, in the meantime, move from the catalyst layer, through the current collector and separator plate to the cathode side. After reaching the cathode side, protons will then recombine with electrons to form hydrogen. The hydrogen gas then flows across the cathode current collector and separator plates to leave the cell.[3]

The cell reactions are summarized below:

Anode reaction: $H_2O \rightarrow 1/2O_2 + 2e^- + 2H^+$

Cathode reaction: $2\mathrm{H}_+ + 2\mathrm{e}^- \rightarrow \mathrm{H}_2$

There are two definitions of free energy and both are related to work done by the system. The Helmholtz free energy is the maximum amount of work that can be obtained from a system under perfectly reversible conditions, and is used for thermodynamic calculations of heat engines. Gibbs free energy corresponds to the net-work that can be done by a system. For an electrochemical cell working reversibly at constant temperature and pressure, the net-work is equal to the electrical work.[15]

Combining the two equations, one can get the total reaction for water electrolysis which is simply the reverse of fuel cell reaction[15]:

Total reaction: $H_2O + 237.2\frac{KJ}{mol}electricity + 48.6\frac{KJ}{mol}heat \rightarrow \frac{1}{2}O_2 + H_2$

To split one mole H_2O, one needs to add 237.2KJ electricity as well as 48.6KJ heat. Actually, the heat is also added by means of electricity since ohmic resistance of an electrolyzer cell also generates heat. Thus the overall energy applied should be $237.2\frac{KJ}{mol} + 48.6\frac{KJ}{mol} = 285.8\frac{KJ}{mol}$. The minimum necessary cell voltage for the start-up of electrolysis, E_{cell} , is given

under standard conditions (P, T constant) by the following equation: Merging electrochemistry with thermodynamics gives this formula below:

$$\Delta H = -nFE_{cell}$$

Where ΔH means the change of enthalpy, n means the number of electron transfer during the reaction, E_{cell} , which corresponding to the minimum necessary cell voltage for the start-up of electrolysis, is equal to 1.48V under standard conditions (25°C,1bar).[16] However, in reality, the actual operational voltage should be larger than 1.48V, since activation energy as well as some losses exist during operation.[15]

In an electrochemical cell, under open circuit condition, the voltage across the cell should be equal to the thermodynamic equilibrium potential theoretically. However, when closing the circuit, the so-called over-potential lead to a decrease (galvanic cell) or to an increase (electrolysis cell) of the voltage. This happens due to the presence of kinetic and transport mechanisms that introduce irreversibility to the electrochemical process. In PEM fuel cell the cell voltage tends to decrease with increasing current density, while in PEM electrolysis cell voltage increases.[17]

The polarization curve is a plot of cell voltage versus current density for a specific electrochemical system which describes the irreversibility discussed above. A typical polarization curve for water electrolysis is shown in the following graph.

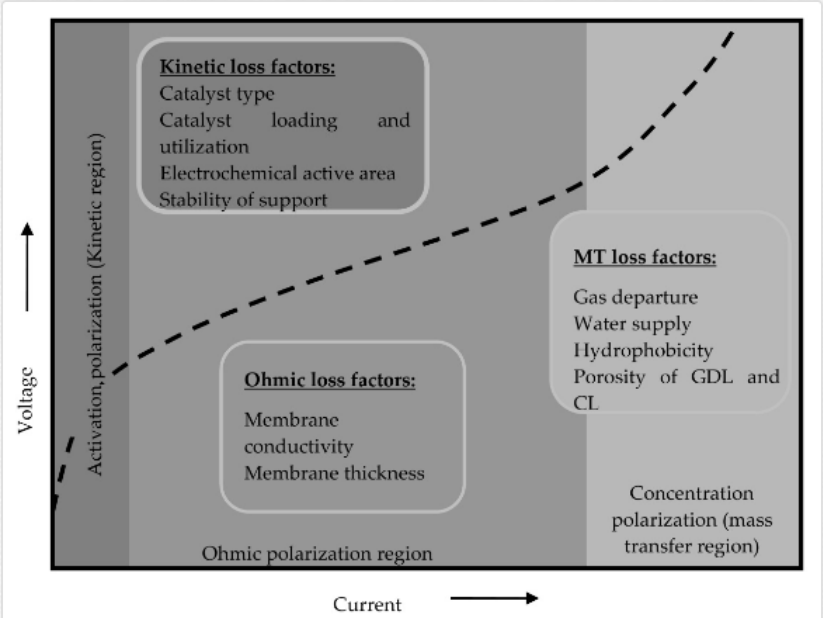

Figure 2-2 Polarization curve for water electrolysis. [18]

The activation over-potential or kinetic loss in an eletrolyzer occurs mainly due to the sluggishness in oxygen evolution kinetics at the anode side and can be minimized by increasing the catalyst activity. [18] A couple of inspects, such as catalyst type, catalyst loading, the electrochemical active area and the stability of the catalyst support determine the electrolyzer performance in the activation region of the polarization curve.

In the ohmic region, the performance of the electrolyzer depends on the conductivity of the stack components. One important factor affecting the ohmic loss is the electrical conductivity of the stack especially the bipolar plates. As for a single cell, ionic conductivity of the membrane is the dominant factor affecting the ohmic loss. Besides, factors such as contact resistance between the MEA sublayers and the compression pressure of the stack, may as well affect the ohmic loss in the electrolyzer stack.[18]

As the current increasing, the mass transfer limitation or concentration limitation becomes the dominant factor. Mass transfer limitation mainly corresponding to two aspects, the first one is gas diffusion and the second one is the water transportation inside the MEA. Porosity, pore size, PTFE content in the membrane and compression pressure plays an important role in the mass transfer region. Properties such as PTFE content (hydrophobicity), pore size, porosity and compression pressure determine the electrolyzer performance in the mass transfer region.[18]

2.2 Oxygen evolution reaction

Compared to the fast reaction of hydrogen evolution reaction on the cathode side, oxygen evolution reaction typically has much slower reaction kinetic and complex reaction mechanism. Many studies have proposed the mechanism of oxygen evolution reaction. However, the actual reaction mechanism has not been understood completely. Here I will mention one of the mechanism of OER in acid media as shown below.[19]

Table 1 Possible reaction mechanism of OER (b stands for Tafel slope)

$S + H_2O \rightarrow S - OH + H^+ + e^-$	$b = 120mV/dec$	(2a)
$S - OH \rightarrow S - O + H^+ + e^-$	$b = 40mV/dec$	$(2b)$
$S - O + S - O \rightarrow 2S + O_2$	$b = 30mV/dec$	$(2c)$

In recent studies, it has been proposed that the rate determining step in OER is the formation of hydroperoxide-type (OOH) species on metal surfaces which are partly-oxidized, according to deprotonation process, shown in equation (2d).[20]

$$S - O_{ads} + H_2O \rightarrow S - OOH_{ads} + H^+ + e^- \qquad (2d)$$

The reaction kenetics are strongly influenced by the surface morphology and catalyst material properties. Some study proposed that S is an active site related to a topological defect on the film and correlated a strong S–OH bond with cracked oxide film that allows more protons to penetrate into the bulk along the defects.[21] That is to say, the reaction is mostly happens on surface defects, or an active site, thus the reaction rate will depend on the number of available sites on the electrode surface.[20] In fact, other complex factors could influence the kinetics of iridium-based catalysts. Therefore, only *in-situ* spectroscopy and other sophisticated characterization method can really investigate the OER mechanism of Ir-based catalysts.

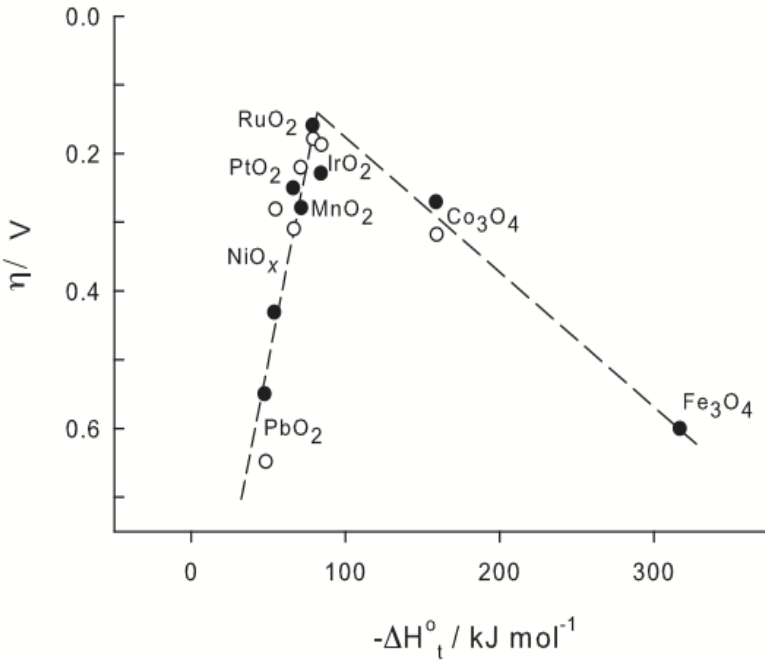

Figure 2-3 Volcano plot of electrocatalytic activity for oxygen evolution reaction of different oxide electrodes. (o) and (●) correlate to alkaline and acid solutions respectively. y axis correlates to reaction rate and x axis associates with properties such as enthalpy of the lower to higher oxide transition.[15]

According to Sabatier principle, the interaction between the catalyst and the substrate should be "just right", that is neither too strong nor too weak. If the interaction is too weak the

substrate will fail to bind to the catalyst and no reaction will take place. On the other hand, if the interaction is too strong product fails to dissociate.[22]

As shown in Figure 2-3, the catalytic activity order for oxygen evolution reaction (OER) were found to be: $Ru \approx Ir > Pd > Rh > Pt > Au > Nb$.[23] Both ruthenium and iridium (actually ruthenium oxide and iridium oxide) have long been identified as optimal catalyst materials for the oxygen evolution reaction in PEM electrolysis.

2.3 Catalyst for oxygen evolution reaction

2.3.1 Requirements for oxygen evolution reaction catalyst

Apart from a high OER activity, a suitable catalyst should also fulfill other requirements. First of all, a large electrochemical surface area is usually needed because it minimizes the amount of catalyst, especially for scarce noble metal catalysts, e.g. iridium or ruthenium. Besides, a high electrical conductivity under high potential condition is also required to minimize ohmic loss.[20]

In a PEM water electrolyzer cell, the anode catalyst exposed not only to an acidic environment, but also severe oxidative medium. Therefore, another requirement for the improvement of advanced catalyst is the corrosion resistance for both catalyst and catalyst support(substrate). Similar to ORR, the reaction path via two electrons instead of four electrons is also possible, resulting in production of peroxide species.[19]

Another important factor is the wettability or removal of gas bubble. Due to oxygen or hydrogen formation on the surface of the catalyst active sites, gas bubbles forms on both side of the electrolyzer cell, which won't be detached from the surface until it grows big enough.[24] As a result, the surface of the catalyst is covered by gas bubbles, which block the electron transfer process so that part of the surface area may not participate in the electrochemical reaction. Increasing the hydrophilicity of the catalyst leads to easier gas removal.[24] Also, developing a catalyst with optimized pore size would be able to reduce gas bubble formation and promote gas bubble detachment.

Stability is another important requirement for electrocatalyst. In PEM water electrolyzer, there are many factors which influence the degradation process of the eletrocatalyst. Possible degradation mechanisms are shown below. [25]

- Catalyst agglomeration
- Corrosion of electrocatalyst support
- Contamination in catalyst or membrane
- Membrane puncture
    - Manufacture
    - Hotspot
    - Mechanical degradation

Most of the degradation mechanisms are quite self-explaining. Due to high applied potential for PEM water electrolyzer, the support material may suffer from corrosion problem. As the water splitting reaction goes on, more and more gas bubbles are produced which could induce mechanical strength in electrolyzer cell that may lead to membrane puncture. The degradation mechanisms (coming from fuel cell research) are just assumptions and need more research to prove the authenticity.

2.3.2 singel-metal and Bimetal oxide electrocatalyst

Water electrolysis performed in acidic Proton Exchange Membrane water electrolyzer (PEMWE) shows a superior performance compared to alkaline water electrolyzer which is a well-developed technology for producing hydrogen. The advantages are mainly shown in the following aspects: PEMWE could be operated in higher current density due to low electrolyte conductivity and could be operate at high pressure which lower the energy input for compressing hydrogen gas. One of the key challenges for PEM electrolyzer is to find a proper oxygen evolution reaction (OER) catalyst which offering superior kinetics and stability under harsh (acidic and oxidizing) environment since anode reaction is much slower than cathode reaction (hydrogen evolution reaction possess superior kinetics on Pt-based catalyst). As discussed in the previous section, iridium and ruthenium are the best feasible options for OER, and iridium is the best compromise between catalyst activity and stability. However, both iridium and ruthenium are extremely expensive and one of the rarest elements on earth (side product of Platinum mining). The production rate for iridium and ruthenium are limited by platinum production rate. Thus, to achieve large-scale production, the noble metals iridium and ruthenium has to be reduced by around one order of magnitude.[26] Although early studies are focusing on noble metal catalyst, it must be specified that under high potential, most metal electrode will form hydrous oxide layer on the surface and can extend into the bulk to different degrees.[27,28]

Although RuO2 has the highest OER activity of all the materials, as shown in the volcano plot, in acid media, under higher potential (>1.4 V), RuO_2 is thermodynamically favored to be oxidized to RuO_4, which serve as a corrosion product on the electrode surface and then dissolve into the electrolyte, thus loss its catalytic activity, as shown in the figure below.[3] On the contrary, iridium oxide not only has a similar OER activity but also has better stability toward corrosion. That doesn't means that iridium oxide is the better choice for OER due to its scarcity in the earth. Since ruthenium is much abundant than iridium, scientist are trying to find alternatives to stabilize RuO_x. When mixing RuO_2 with IrO_2, Stucki and Kötz hypothesized the band mixing between the IrO_2 and RuO_2 orbitals thus the electrons available on IrO_2 sites could be shared with RuO_2 which raises the potential for Ruthenium oxidation.[29] By this means, rutile phase RuO_2 was stabilized by IrO_2 from its high dissolution rate.

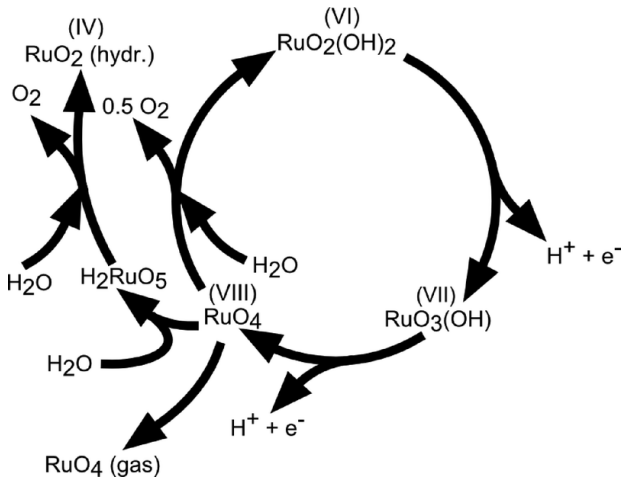

Figure 2-4 Model for the oxygen evolution and corrosion on Ru and RuO_2 electrodes.[30]

The other important electrocatalyst is Iridium oxide. Iridium shows stability towards high anodic potential in harsh acidic environment, high electrical conductivity[31,32] and slightly lower OER activity compare to Ruthenium oxide.[33]

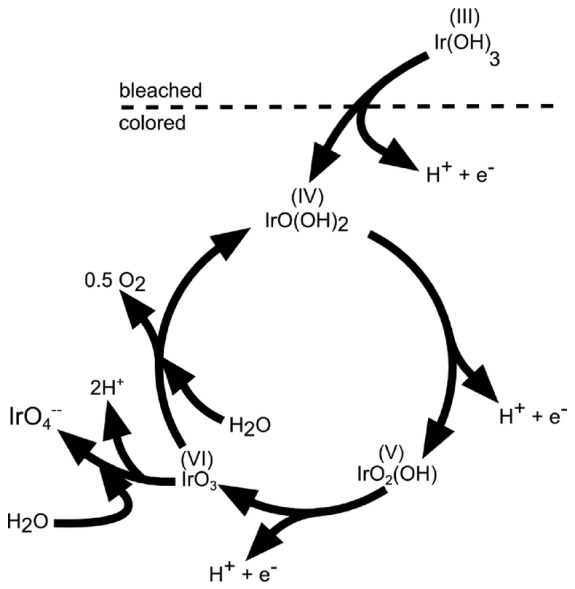

Figure 2-5 Scheme of the OER on anodically grown hydrous iridium oxide films.[27]

Upon potential cycling of an iridium metal electrode, a hydrous oxide layer forms at the metal–electrolyte interface, which grows into the bulk with the number of applied cycles.[27] Kötz and coworkers proposed an OER mechanism on anodic grown oxide film, as shown in the Figure 2-5. As we can see, the reaction goes through several continuously deprotonating steps with iridium in a 3+ valence state at potentials below 1V (RHE). It is assumed that an unstable VI+ intermediate oxidation state (IrO_3) exist before dissociation to tetravalent state at the starting point of cycle.[19] This illustrated mechanism is consistent with the electrochemical oxide path, as described in table 1.

2.3.3 Supported material and surfactants

Many studies have reported that Antimony-doped tin dioxide (ATO) is a good OER catalyst support due to its morphology and good conductivity.[34] In this study, aerogel structure ATO, NTO (provided by Armines Frnace) are used as the supporting material.

Regarding to the morphology, the catalyst supports with mesopores are preferable for OER catalyst since the optimum iridium particle size is in a range of a few nanometers. Moreover, mesopores allow good iridium nanoparticle distribution while avoiding pore obstruction. [34]

With respect to these considerations, SnO_2 aerogels used in this thesis show very interesting morphology or topography. The specific area of SnO_2 aerogels are approximately 90 m^2 g^{-1} with proper pore size distribution and medium or large mesopores (25-45 nm) and also

negligible micropores. As we can see from Figure 2-6, the overall figure of Nb-doped tin dioxide has the similar morphology as pure tin dioxide while Sb-doped tin dioxide shows an airy morphology with a three dimensional network made up of interconnected particles. [34]

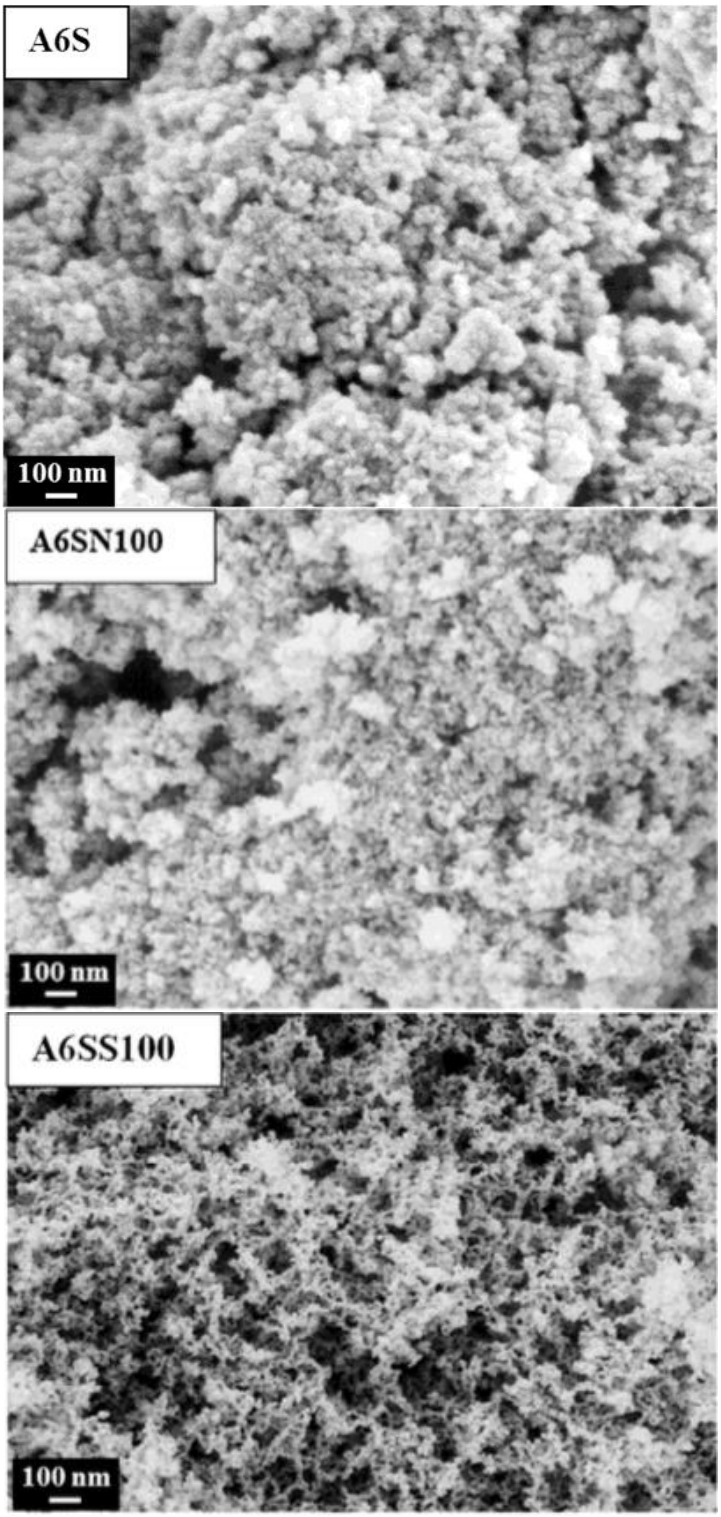

Figure 2-6 SEM images of aerogels: pure SnO_2, NTO (Nb 10 at%), ATO (Sb 10 at%), calcined for 5 h at 600 ^{O}C in air.[34]

Regarding the electronic conductivity, only ATO has high enough electronic conductivity of approximately 1 S/cm (Sb 5 at%). For NTO, the conductivity is only 4.5×10^{-5} S/cm. The support material used in this thesis is ATO (Sb 10 at%) and NTO (Nb 10 at%) describe above from MINES ParisTech.

Compared to metals, semiconductors provide much lower charge carrier concentration, and thus, a large space charge layer is formed at the surface. In general, at anodic potentials typical for the OER, the potential drop in the space charge layer will be negligible for the p-type semiconductor due to the accumulation of holes at the surface. In contrast, for n-type semiconductors, the space charge layer at the interface leads to an additional barrier for charge carriers. Therefore, p-type semiconducting oxides or metallic-like oxide conductors should be more suitable catalyst materials for the OER than n-type semiconductors.[35]

Chemical changes are initiated to convert the precursor ($IrCl_3$) to iridium metal atoms by the reducing agent, these metal atoms then merge into suitable supported materials/or stabilizer. In our case, $IrCl_3$ is reduced by $NaBH_4$ to produce iridium nanoparticles:[36]

$$8Ir^{3+} + 3NaBH_4 + 24OH^- \rightarrow 8Ir + 3NaBO_2 + 18H_2O$$

Particle growth is usually confined by the presence of a protection surfactant. Supported and size-controlled nanoparticles could then be produced.

The support material for the metal nanoparticles turns out to be as important as the nanoparticles for providing their dispersion and stability. It also provides electrical conductivity when used as electrode. In addition to electrical conductivity, supporting materials must have some important properties such as high surface area, hydrophobicity, morphology, porosity, corrosion-resistance for the choice as a good catalyst support.[37]

Surfactants are compounds that could lower the surface tension between two liquid or between a liquid and a solid. It is extremely important for the catalyst synthesis process. In wet chemical synthesis, surfactants are used to stabilize nanoparticles against aggregation by steric repulsion, thus nanoparticles with only few nanometers size could be obtained. Surfactants are usually organic compounds that are amphiphilic, which means they contain both hydrophobic groups (tails) as well as hydrophilic groups (heads). The function of

surfactant used in precious metal nanoparticle synthesis is that it can prevent aggregation of precious metal nanoparticles.[37]

For example, the platinum nanoparticles are synthesized using a colloid method by the reduction of a platinum precursor (H_2PtCl_6) in alcohol with the presence of a surfactant to avoid aggregation (Humphrey and et al. 2007, Zhang and et al. 2007). As the particles nucleate and grow, the hydrophilic heads of the surfactant will attach to the plantinum particles while the hydrophobic tails will attach to the solvent. Thus the particles are kept within the surfactant which is porous enough to allow growth to various sized form 2 to 8 nm and various shapes (Bratlie and et al. 2007). The iridium catalyst synthesis method used in this work is similar to the colloid method described above. Figure 2-7 shows the schematic flow diagram of iridium catalyst synthesis procedure.

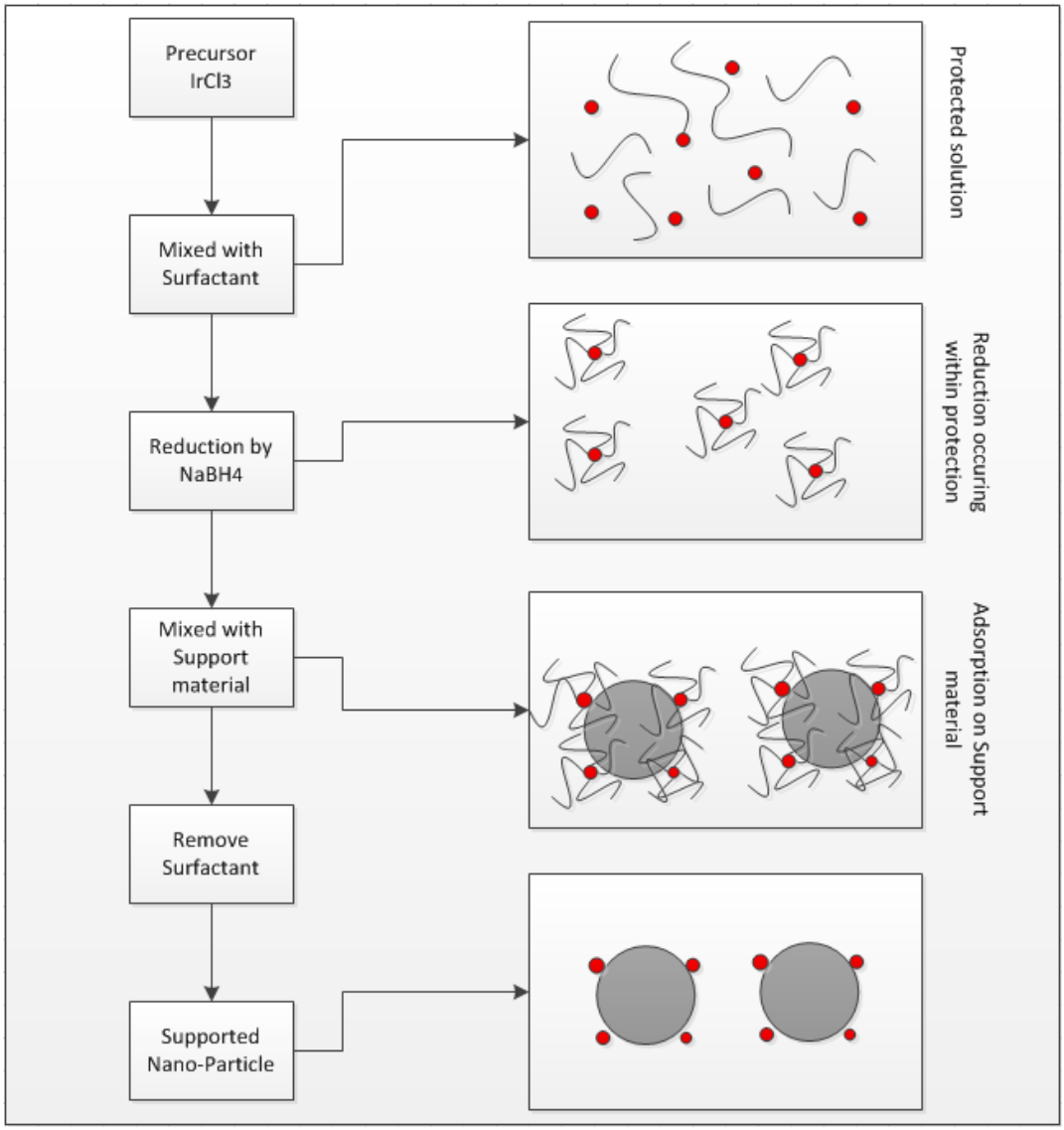

Figure 2-7 Wet chemical synthesis route shown schematically in flow chart

In the synthesis route, all the chemicals were anhydrous and all the experiment apparatus (flasks) were filled with Nitrogen gas before using to make sure that the whole process was in water free condition. That was because water may affect the function of the surfactant and change the structure of the nanoparticles.

2.4 Electrochemical and physical characterization

2.4.1 iR compensation

An overview of an electrochemical half-cell equivalent circuit is shown in the following graph (the reasons why we use this circuit will be discussed in section 2.4.3). The electrochemical measurement was carried out in a potentiostat with three-electrode setup. The potentiostat is a instrument that is designed to control the working electrode (WE) potential relative to a reference electrode (RE) for electrochemical measurements. In order to control the potential, the potentiostat will alter the potential of the counter electrode (CE) with respect to WE (which is the virtual ground). The potential of the CE is adjusted to the required voltage within the compliance voltage limits in order to keep the potential difference between the RE and the WE to be exactly the user-defined value.

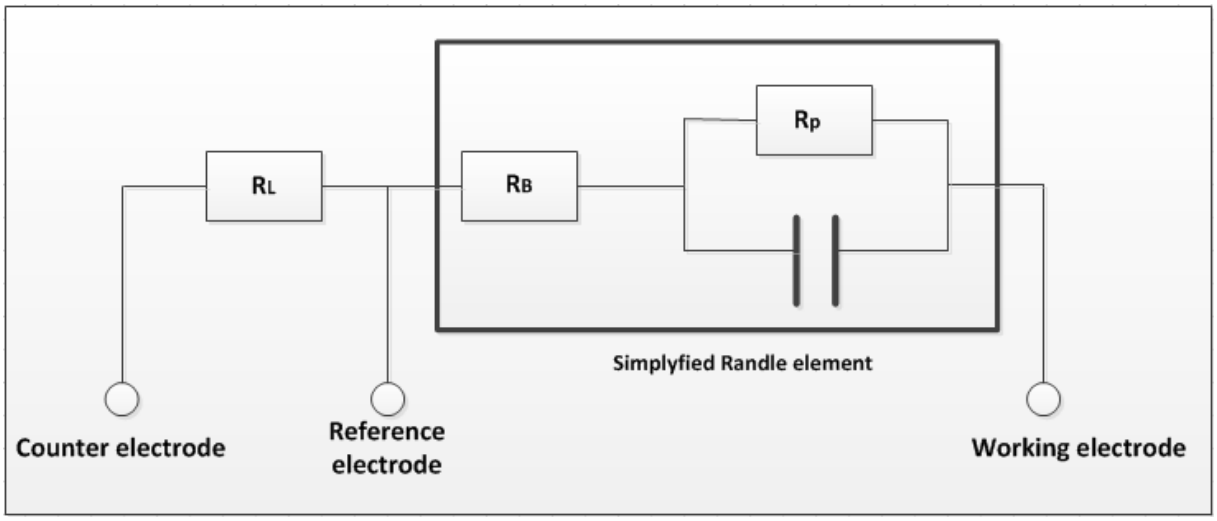

Figure 2-8 Simplified electrochemical half-cell used in the electrochemical measurement, R_L corresponds to the solution resistance and R_B corresponding to the solution resistance between the Reference electrode and the Working electrode, R_P is the charge transfer resistance of the corresponding catalyst reaction, and the capacitance corresponding to the double layer capacitance. The double-layer capacitance is in parallel with the charge-transfer resistance.

However, in reality, the reference electrode is always located at a distance relative to the working electrode that the solution between will introduce an extra resistance (R_B) which can't be compensate by the potentiostat. That means whenever a current (i) passing through the circuit described in Figure 2, there is always an uncompensated resistance which leads to an additional voltage drop called iR drop, given by:

$$V_{iR} = i \cdot R_B$$

In order to get the value of R_B, an EIS module was employed as discussed in section 2.4.3.

2.4.2 Oxygen evolution reaction (OER) activity determination

In the kinetic region of an electrochemical reaction, the logarithm of current varies linearly with overpotential (when overpotential is large enough), which could be derived from Butler-Volmer equation. The slope of the potential vs. logarithm current line (normally using mV dec^{-1} as unit) is called Tafel slope. In order to compare/define the catalyst activity, two parameters need to be considered. One is the Tafel slop, which describe the kinetics of the electrochemical reaction:

$$\frac{d\eta}{dlg(j)} = \frac{\alpha z F}{2.3 \times RT}$$

It can be simplified as the following equation:

$$\eta = a + b\log|i| = b\log\frac{|i|}{|i_0|}$$

Where F is the faraday constant, z is the charge transfer number, α is the reaction transfer coefficient, η stands for overpotential, *b* is the Tafel slope and *i* is the current density. And the exchange current density i_0 is the current at equilibrium potential. For electrochemical reaction, the electron transfer processes continue at electrode/solution interface in both anode and cathode sides at the equilibrium potential. However, the anodic current is balanced by the cathodic current, thus the net current is equal to zero. The ongoing current in both anode and cathode sides is called the exchange current density, which depends on the catalysts type, catalyst loading, surface structure of the electrode and etc. At a specific temperature, the Tafel slope depends only on the reaction mechanism, which relates to the product of charge transfer number z and the reaction transfer coefficient α of the rate determining step (RDS). The Tafel

slope is largely used, especially from application point of view, to compare the performance of different OER catalyst.

However, we need another parameter to fully determine the catalyst activity because two catalyst with the same Tafel slope could have different exchange current density, e.g. current at 1.48V (vs RHE) as an activity parameter for OER. Table 2 gives the possible parameters that can be used in combination with Tafel slope to describe the catalyst activity of different catalysts.

Table 2 Three parameters in combination with Tafel-slop to describe the catalytic activity of different catalyst material for OER.[19]

Parameter	Symbol
Exchange current density	j_0
Potential at a defined current density	$\emptyset(j), e.g. at\ 5mA/cm^2$
Current density at a defined potential	$j(\emptyset), e.g. at\ 1.48V$

However, for high irreversible reaction like OER, using the exchange current density as the intrinsic parameter for OER is not possible since the experimental determination is highly incorrect. Due to the logarithm scale of the current axis, a very small error in determining the Tafel slope, e.g. derived from iR compensation or linear fitting, can lead to large difference in determining exchange current density.[19]

The mass activity could be calculated by normalizing the current with respect to the mass of noble metal catalyst used. This is quite simple and effective way to normalize electrochemical catalyst since it is directly related to the cost of the electrolyzer electrode. In this thesis, 10 μL of a 1.2 mg/ml catalyst ink was coated on the RDE surface using a transfer pipette. The catalyst ink was sonicated each time before coating on the RDE to get a homogenous dispersion, thus, 12 µg (1.2E-5 g) electrocatalyst was coated on the RDE surface. So the catalyst mass activity can be written as the following equation:

$$Mass\ activity[A/g] = \frac{I[A]}{0.000012g \times x_{catalyst}}$$

The noble metal loading on ATO is given in weight fraction and written as $x_{catalyst}$. For supported catalyst analyzed in this thesis, the noble metal loading $x_{catalyst}$ was set to be 30%. However, limited to synthesis condition, the practical noble metal loading was normally lower than 30 % and could be determined by EDX measurement. Another way to describe the catalyst activity is the specific area activity which is shown in the equation below:

$$Specific\ area\ activity\left[\frac{mA}{cm^2}\right] = \frac{I[A] * 1000\frac{[mA]}{[A]}}{0.196cm^2}$$

The surface area of the GC-RDE is equal to 0.196cm^2.

2.4.3 Electrochemical impedance spectroscopy

Electrochemical impedance spectroscopy is a powerful and cost effective tool for both Fuel cell and Electrolyzer characterizations. There are three types of voltage losses in Electrolyzer which are charge transfer activation or kinetic losses, ion and electron transfer or ohmic losses and mass transfer losses. EIS is an experimental technique that could distinguish and quantify these losses by applying an equivalent circuit model where the electrochemical processes of eletrolyzer cell are represented by a network of resistors, capacitors and inductors. [38]

In the RDE, only the half-cell reaction was considered, that is the oxygen evolution reaction. As we all know, the equivalent circuit of a typical interfacial electrochemical reaction in presence of semi-infinite linear diffusion of electroactive particles to flat electrodes is simplified as "Randles" circuit shown in Figure 2-9.

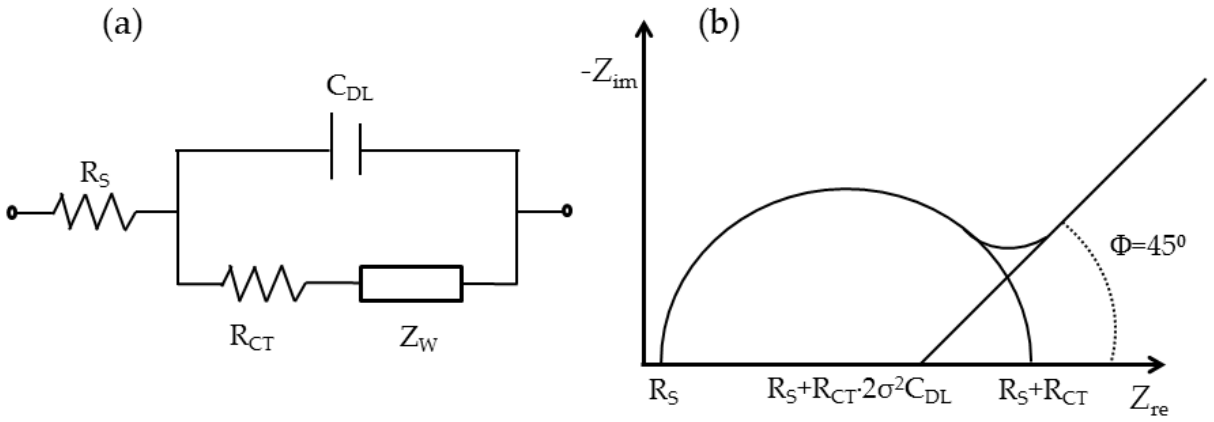

Figure 2-9 Randles circuit schematic (a) and Nyquist plot (b) of its frequency response Where R_S is the electrolyte resistance, C_{DL} is the double layer capacitance and R_{CT} is the charge transfer resistance and a specific electrochemical element of diffusion Z_W, which is also called Warburg element $\boldsymbol{Z_W = A_W/(j\omega)^{0.5}}$.[39]

R_S is inserted as a series element in the electrochemical cell because all the current passes through the uncompensated solution. The parallel elements are introduced since the total current through the electrodes is the combination of faradic process and the double layer charging process. R_{CT} corresponds to the charge transfer resistance and C_{DL} corresponds to the double layer charging capacitance. Z_W represents the diffusion of redox probe. R_S and Z_W represent bulk properties of the electrolyte and diffusion of the redox probe, while C_{DL} and R_{CT} depend on dielectric and insulating features at the electrode/electrolyte interface.

EIS data for electrochemical cells such as electrolyzer are usually represented in Nyquist plot and Bode plot where Nyquist plot represented imaginary impedance versus the real impedance and Bode plot shows the magnitude and phase as a function of frequency.

The Nyquist plot (Shown in Fig. 2-9(b)) is the best way to visualize and determinate the Randles EC elements. The semicircle observed at high frequencies corresponds to the electron transfer limited process and linear part at lower frequencies represents the diffusion limited process. The intercept of semicircle at high frequencies with the Z_{re} axis is equal to Rs (short circuit for the capacitor), while extrapolation of semicircle to lower frequencies into another intercept with Z_{re} axis is equivalent to $R_S + R_{CT}$. The double-layer capacitance C_{DL} can be calculated from the frequency at the maximum of the semicircle.

3. Experiment

3.1 Catalyst preparation

3.1.1 Synthesis of supported catalyst

Commercially available reagents were used as received in the synthesis of supported iridium catalyst and bimetallic IrRu catalyst.

Table 3 Chemicals and equipment for catalyst synthesis

Chemicals	Equipment
-$IrCl_3$, anhydrous, Ir 62% min	-Three-necked round bottom flask
-$RuCl_3$, anhydrous, Ru 47% min	-Magnetic stirrer, SCHOTT
-ATO, Sb 10 %at. MINES ParisTech	Instruments GmbH
-NTO, 10 %at. MINES ParisTech	-Centrifuge, ThemoFisher Scientific
-CTAB, VWR	-Ultrasonic bath, VWR
-$NaBH_4$, VWR	-Muffle Furnace
-NH_4VO_3, ACS, 99.0%	
-Ethanol, anhydrous, max 0.01% H_2O	

The electrocatalysts were synthesized using the so-called wet chemical synthesis method. The term wet chemical synthesis method emerged in contrast to conventional solid state synthesis method. It uses liquid phase at one of the synthesis process stages. The main advantages of the wet chemical synthesis method(compare to solid state synthesis) is that its products have much smaller grain size and usually lower temperature and shorter time for phase formation.

The supported catalyst under investigation are: antimony doped tin dioxide (ATO) supported iridium catalyst with/without H_2O_2 oxidation, niobium doped tin dioxide (NTO) supported iridium catalyst and ATO supported vanadium iridium catalyst.

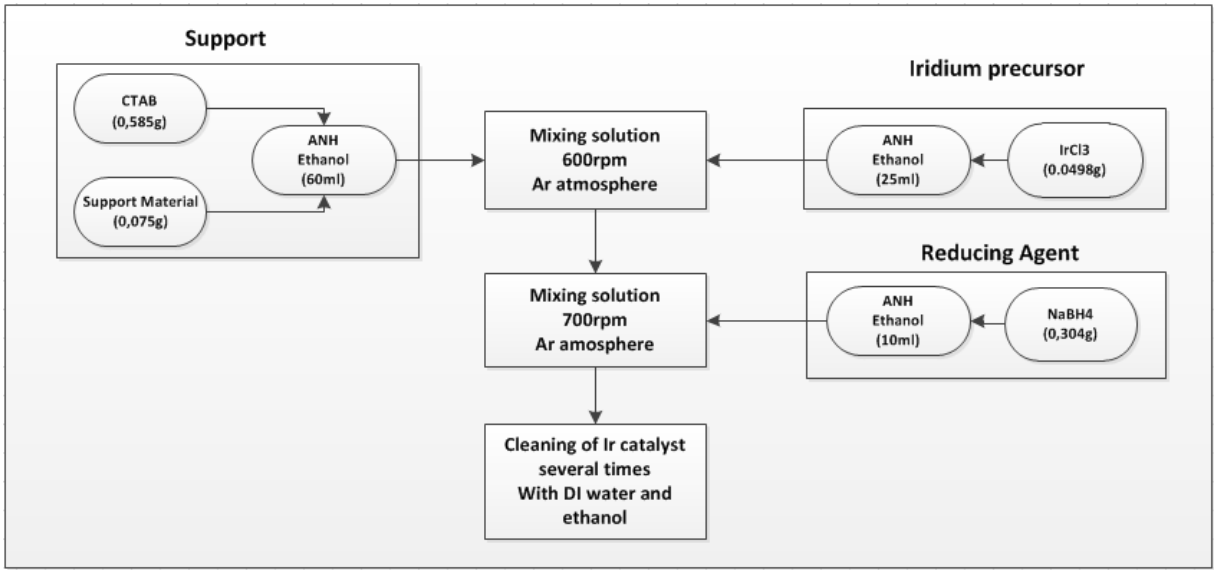

Figure 3-1 Scheme of the synthesis procedure of supported 30 wt% iridium catalyst. DI = deionized water, ANH = anhydrous and CTAB = cenltrimethylammonium bromide.

The ATO supported iridium catalyst is carried out using a wet-chemical method which is developed and used in the former research conducted by the Li Wang, et al. at German Aerospace Center. 0.585 g cetyltrimethylammonium bromide (CTAB) and 0.075 g Sb-doped SnO_2 (ATO) was dissolved in 60 ml anhydrous ethanol solution (99.9%) in a three-necked round bottom flask with Argon flowing. Then the solution was stirred for 30 minutes to get a homogeneous dispersion. After that, 0.0498 g anhydrous $IrCl_3$ was dispersed in 25 mL anhydrous ethanol using an ultrasonic bath. The $IrCl_3$ solution was then transfer to ATO solution and left at room temperature with 500rpm magnetic stirring and argon flowing for 3 hours. The weight ratio between iridium and ATO is exactly 3:7. In order to reduce the $IrCl_3$ to iridium nanoparticles, 0.304 g sodium borohydride ($NaBH_4$) was then dispersed in 10 mL anhydrous ethanol solution by sonication for 10 minutes and transfer to the ATO dispersion. The solution was then left at room temperature with 700 rpm magnetic stirring overnight. The ATO supported iridium catalyst was then centrifuged in ethanol and deionized water for 3 times and 5 times respectively to get rid of CTAB and the residual non-reduced $IrCl_3$. At the end, the catalyst was dried overnight in an oven at 40°C.

The same procedure was applied for Nb-doped tin dioxide catalyst synthesis.

As for ATO supported iridium vanadium catalyst, an additional 0.032g ammonia vanadium oxide powder was added to iridium precursor to achieve mass ratio (vanadium to iridium) of 3:7.

3.1.2 Unsupported catalyst preparation

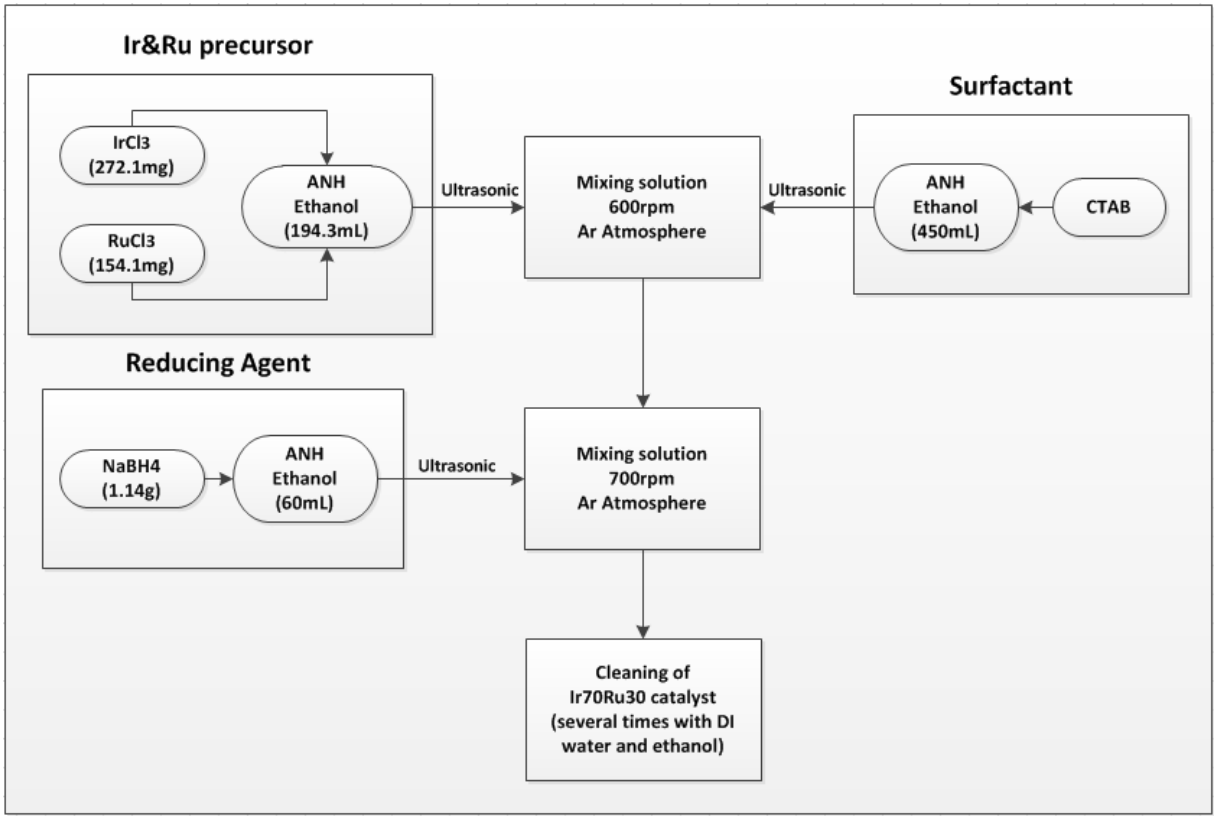

Figure 3-2 Scheme of the synthesis procedure of Iridium Ruthenium catalyst (70 wt% Ir). DI = deionized water, ANH = anhydrous and CTAB = cenltrimethylammonium bromide.

The synthesis of bimetallic IrRu catalyst is carried out using the same method as the supported catalyst preparation. 4.3875 g CTAB was dissolved in 450 ml anhydrous ethanol solution (99.9%) in a three-necked round bottom flask with Argon flowing. After that, 271.1 mg anhydrous $IrCl_3$ and 154.1 mg $RuCl_3$ were dispersed in 194.3 ml anhydrous ethanol and sonicated for 10 minutes. The weight ratio between iridium and ruthenium is exactly 7:3. Then transfer the IrRu solution to the surfactant solution and left at room temperature with 500 rpm magnetic stirring and argon flow for half an hour. In order to reduce the $IrCl_3$ and $RuCl_3$ to iridium and ruthenium nanoparticles, 1.14 g sodium borohydride ($NaBH_4$) was then dispersed in 60 mL anhydrous ethanol by sonication for 10 minutes and added to the surfactant solution. The solution was then left at room temperature overnight with 700 rpm magnetic stirring and argon flow. The bimetallic IrRu catalyst was then centrifuged in ethanol and deionized water for 3 times and 5 times respectively to get rid of CTAB and the residual non-reduced $IrCl_3$. At the end, the catalyst was dried overnight in an oven at 40°C.

The resulting product was labeled as $Ir_{70}Ru_{30}$ since the weight ratio of iridium to ruthenium was 7:3.

3.2 Physical and Electrochemical characterization

Table 4 Equipment and chemicals for electrode preparation electrochemical measurement

Chemical	Equipment
-Alumina Suspension for polishing, 0.05μm	-Ultrasonic bath, VWR
-Ultrapure water, Alfa Aesar	-PGSTAT12 potentiostat
-Ethanol, 99%, VWR	-RHE electrode
-Nafion® perfluorinated resin solution. Sigma-Aldrich	-Pt counter electrode
-Sulfuric acid 0.5M in aqueous solution, VWR	-GC rotating disc electrode, Pine Research Instruments
	-Electrode speed control, Pine Research Instruments
	-Zahner potentiostat with EIS module

3.2.1 Catalyst ink and electrode preparation

Weigh 10 mg catalyst powder into a small glass vial. 8.3 mL ultra-pure water as well as 40 μL Nafion solution was pipetted into the glass container. The Nafion® ionomer solution was used to simulate the real working condition of anode catalyst in PEM water electrolyzer and to prevent the catalyst from falling off.

In order to get a well-mixed aqueous catalyst ink suspension, the glass vial is then put into the ultra-sonication bath with controlling temperature (less than 40°C) for 30 minutes.

In PEM water electrolyzer, the anode potential has to be larger than 1.48V vs. RHE as described in section 2.1 in order to start producing oxygen. Therefore, Au-RDE is not suitable for studying iridium based anode catalyst for PEMWE because Au is thermodynamically unstable at 1.46 vs. RHE. A mirror liked surface Glassy carbon (GC) rotation disk electrode (RDE) was prepared for electrochemical measurement. The GC electrode was polished using 0.05 μm γ-Al_2O_3 until a mirror liked surface was formed. Then the electrode surface was washed using deionized water in ultrasonic for at least 10 seconds.

10μL catalyst ink was pipetted and coated onto the mirror like GC electrode surface with a geometric area of 0.196 cm^2. The catalyst modified electrode was then put into a drying chamber filling with Argon gas for 20 minutes. After that, put it to the electrochemical cell for further measurements.

In summary, the catalyst loading is $12\mu g$ calculated in section 2.4.2 and the normalized catalyst loading with respect to electrode surface area is approximately 60 $\mu g/cm^2$.

In this thesis, several supported or unsupported catalysts prepared in this work are characterized electrochemically and physically. As for electrochemical characterization, cyclic voltammetry (CV) was carried out in a three-electrode cell, in which a GC-RDE is used as the working electrode, a reversible hydrogen electrode (RHE) was employed as a reference electrode and a platinum sheet was employed as the counter electrode. To avoid the polarization of the counter electrode, its surface area is many times (>10 times) higher than that of working electrode. All the electrochemical characterization was carried using a PGSTAT12 potentiostat and Zahner potentiostat for EIS. For the physical characterization, different physical method such as SEM, EDX were performed to obtain the morphology, chemical composition, etc.

3.2.2 Physical characterization

Scanning electron microscopy and Energy-dispersive X-ray spectroscopy

The morphology and the composition of the catalysts were studied by scanning electron microscopy (SEM) and Energy-dispersive X-ray (EDX), respectively. The images were recorded based on the energy selective backscattered (ESB) and Secondary electron (SE) detector with an accelerate voltage of 1kV to increase the contrast between iridium and support materials. The loading of iridium on support material was determined by EDX in the following way: as prepared iridium based catalysts were spread on a conductive carbon tape, then we sorted ten areas with different sizes as sample to analyze iridium composition.

3.2.3 OER activity measurement

Electrochemical techniques, such as CV, involves non-equilibrium conditions, and therefore is not expected to have any Nernst response unless the scan rate is relative slow or the reaction rates are relative fast so that equilibrium condition is quickly established. Thus to obtain a reliable current to potential curve the sweep rate was set to be 5 mV/s to lower the double layer charging-discharging effect on the polarization curve. In this thesis, the CV characterization was performed in 0.05M H_2SO_4 electrolyte with RHE as reference electrode and platinum sheet as counter electrode. The OER activity test was firstly performed using the

protocol listed in Table 5. In sequence 1, the potential was swept between 1V to 1.6V vs RHE with scan rate of 5 mV s^{-1}. Then in sequence 2, the potential was swept between 0V to 1.6V vs RHE with scan rate of 20 mV s^{-1}. In the last step, the potential swept is the same as in sequence 1. Number of cycles and the sweep rate are summarized in Table 5. To remove the oxygen generated on the electrode surface, a rotational speed of 1600 rpm/min and N_2 flux were used during Sequence 1 and 3.

Table 5 Electrochemical measurement protocol

Seq. no	Voltage range[V]	Sweep rate [mV/s]	Number of cycles
1	1-1.6	5	3
2	0-1.6	20	10
3	1-1.6	5	3

The reasons why we used these protocols are summarized as following:

1. For sequence No.1, the measured current was not only come from OER because other side reaction occurring at the same time due to high potential, for example, iridium oxidization reaction and some other oxidation reactions from impurities ($IrCl_3$ and CTAB).

2. For sequence No.2 (EC oxidation protocol), it is well known that cyclic voltammetry treatment for pure iridium catalyst in aqueous electrolytes leads to the formation of hydrated oxide films. That is the so called oxidation procedure because the charge transfer through the electrode/electrolyte interface gradually increases to reach a maximum value.[40,41] Thus Sequence No.2 was performed to make sure that surface catalysts were oxidized and also to cleaned the surface to get rid of all the impurities, such as unreduced precursor and CTAB.

3. Sequence No.3 was performed to measure the OER activity which was believed to be the accurate OER activity. And the polarization curve could be obtained in this procedure.

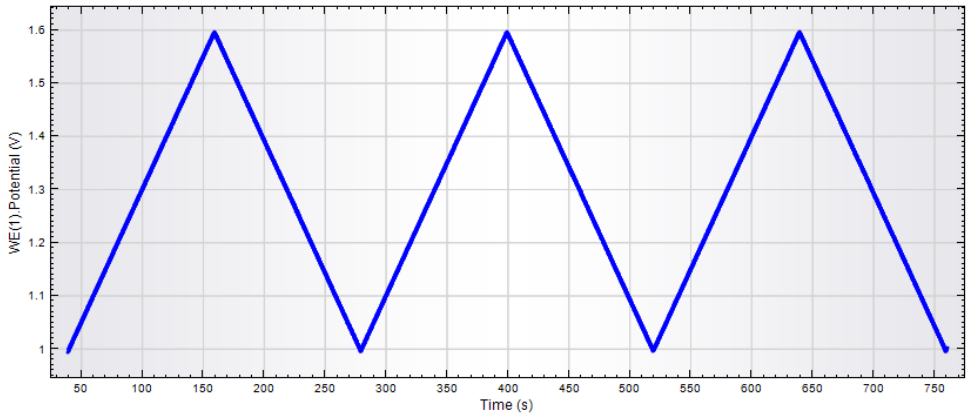

Figure 3-3 OER activity test protocol, approximately 12 minutes, 5 mV/s which is as low as possible to achieve a steady-state condition

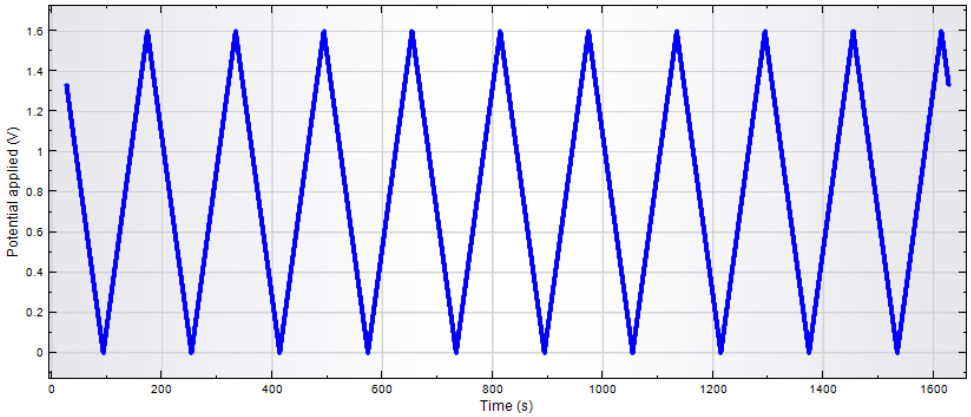

Figure 3-4 Cyclic voltammetry protocol, approximately 27 minutes, 20 mV/s

The potential applied to the RDE was shown in Figures 3-4. Since the actual potentialstat actually applied the potential sweep as a staircase rather than a linear waveform when performing CV, the step size of the staircase waveform was adjusted to a suitable value in order to achieve the stable curve with very little noise.

3.2.4 Stability test

Before stability test, the electrochemical oxidation protocol was performed to make sure that the catalyst on the electrode was fully oxidized and stabilized. The pre-treatment was simply repeating the electrochemical protocol in Table 5, except using only the first two sequences.

To performed the stability test that is closer to the real operating conditions of a PEM water electrolyzer, the potential of the working electrode was recorded constantly with respect to counter electode under a certain current density (galvanostat, 1mA/cm^2) since a PEM water

electrolyzer is usually operated by galvanostatic mode to have a constant hydrogen production rate. The duration of the stability test was set to be 15 hours. The recorded corresponding potential at 1 mA/cm^2 would increase during the measurements. Because the GC electrode had a limited stability towards higher potential (strong carbon corrosion at potential higher than 2.0 V), the upper limit of the potential was set to be 2.0 V to prevent electrode damage from carbon corrosion.

In order to test the stability and durability of the electrocatalyst under condition similar to the operating conditions of PEM water electrolyzer, a special protocol with changed potential ("duty-cycle protocol")[42] were designed and applied for the selected catalysts. First we kept the potential at $E^{0.5}$ (at which the current density was 0.5 mA/cm^2) for 10 min, then the potential was increased by 20 mV ($E^{0.5}$+20 mV) and kept for 10 min. The increasing step was repeated for 5 times until the potential of the final value $E^{0.5}$+100 mV were reached. The whole process is call one duty cycle and is illustrated in figure 3-5.

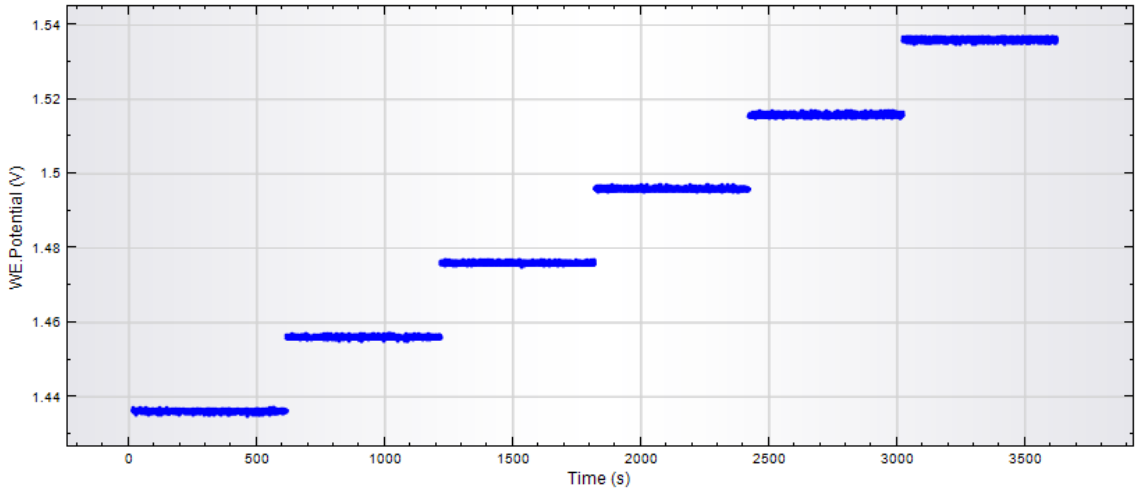

Figure 3-5 Stair-case Duty cycle protocol, the increasing step of Stability test protocol which was repeated for 5 times and working electrode potential increased by 20 mV every 10 minutes.

Duty cycles were repeated for 15 rounds or until the catalyst completely loss its OER activity. After each duty cycle, the OER activity test was performed.

3.2.5 Copper underpotential deposition on Ir-based catalysts

Under-potential deposition refers to the deposition of metals on a foreign metal substrate at potential less negative than the Nernst potential for the reduction of this metal. It can be explained as the binding energy of metal atoms to foreign metal substrate is larger than that of

the atoms to its respective bulk metal. The cupper under-potential deposition (UPD) was widely founded in noble metal such as platinum, ruthenium and gold metal.[43,44,45]

In recent years, iridium metal was reported that under certain potential range, also allows under potential deposition of copper. Furthermore, the presence of copper under-potential deposition only occurs on iridium particle, but not on its thick oxide.[46] The chemical reaction for copper UPD is shown below:

$$Cu^{2+} + 2e^{-} \rightarrow Cu$$

Copper is an ideal metal for UPD on iridium due to the fact that the atomic radius of copper, which is 128 pm, is similar to the atomic radius of iridium, which is equal to 136 pm.[45] Integration of UPD (stripping) peak area allows us to calculate the surface area of iridium metal supposing that one copper atom adsorbed on one surface iridium atom and the number of electron transfer is equal to 2, as shown in the upper reaction.

The Cu UPD experiment was carried out in two electrochemical cells, the background cell and the working cell. A reversible hydrogen electrode (RHE) was used as the reference electrode. The background cell contained 0.5 M sulfuric acid in aqueous solution and purged with nitrogen gas for 20 minutes before each experiment. The working cell was filled with 5mM $CuSO_4$ and 0.5 M H_2SO_4 where both Cu UPD and Over-potential deposition (OPD) were observed. The working cell was purged with argon gas for 20 minutes before each experiment to get rid of oxygen dissolved in the solution.

Catalysts and electrode were prepared according to section 3.2.1 with the catalyst loading of 60 $\mu g/cm^2$. Firstly, the electrode was first kept in the background cell (nitrogen saturated) at 0.05 V vs. RHE for 10 minutes to reduce the reversible iridium oxide species that was formed during the catalyst synthesis procedure. Then the electrode was cycled in the potential window between 0.2 V to 0.72 V vs. RHE for 3 times with scanning rate of 20 mV s^{-1} to obtain the background CV. After that, the electrode was again reduced at constant potential 0.05 V vs. RHE for 10 minutes to make sure that no iridium oxide species exist. Although previously reported that Cu could deposit on electrochemically oxidized Ir electrode,[46] we do not want this to happen to make sure that Cu only deposit on metallic iridium during the experiment.

Secondly, the electrode was transferred to the working cell (5mM $CuSO_4$ dissolved in 0.5 M H_2SO_4, argon saturated). Then the electrode was cycled in the potential window between 0.2 V to 0.72 V vs. RHE for 3 cycles with scanning rate of 20 mV s^{-1} (the same CV protocol as in the background cell) to obtain the copper UPD and UPD-stripping peaks.

The whole test protocol is illustrated in Table 6. Sequence 1, 2 and 3 were performed in background cell. And the electrode was switched to the working cell for sequence 4.

Table 6 Cu UPD experiment CV protocol

Seq. No.	Scan rate / mV s^{-1}	# of cycles	Remarks
1	0	/	Hold potential at 0.05 V for 10 min
2	20	3	Start/end at 0.2 V, upper limit:0.72V
3	0	/	Hold potential at 0.05 V for 10 min
4	20	3	Start at 0.3 V, end at 0.72 V

The charge with respect to the Copper UPD was found by subtraction of the scan in background cell alone and integration of the current vs. voltage curve between the relevant limits which corresponds to the Copper UPD stripping peak position found during the experiment.

3.2.6 Thermal treatment of bimetallic IrRu catalyst

50 mg $Ir_{70}Ru_{30}$ catalyst was carefully weighed and added to the crucible. Then put the crucible into the Muffle ove. The starting temperature was room temperature (roughly 25°C). First the temperature increased linearly with the heating rate of 5°C per minute until the temperature reach (T_{final}-20°C). Then we changed the heating rate to 1°C per minute and wait 20 minutes (to keep temperature stable and eliminate the impact caused by inertia of the heat control system). After that, the temperature T_{final} was reached and annealed for 30 minutes. After that, we cooled down the sample to room temperature with the cooling rate of 5°C per minute. The schematic diagram of the thermal treatment process is shown in Figure 3-6.

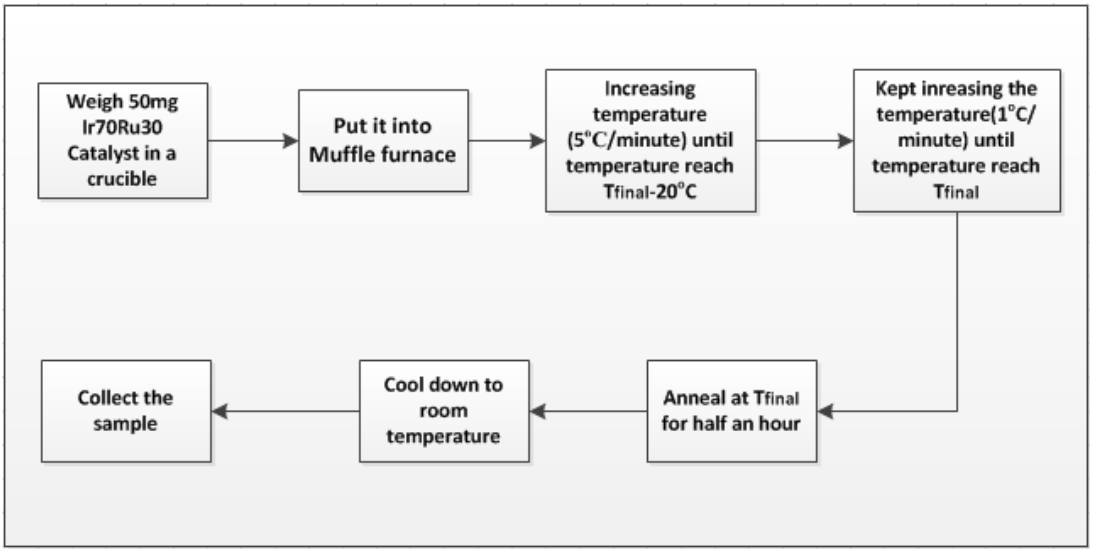

Figure 3-6 Thermal treatment procedure of Ir70Ru30 using Muffle furnace

$Ir_{70}Ru_{30}$ was treated at four different temperatures 300°C, 350°C, 400°C and 450°C and marked as TT300, TT350, TT400 and TT450 respectively. The motivation why we chose those temperatures was to find out the optimized temperature range for thermally oxidized $Ir_{70}Ru_{30}$ to get a better OER activity and stability. It is reported that the temperature for ruthenium to be oxidized to its Rutile phase is between 250°C and 300°C which is 50°C lower than that of iridium (between 300°C and 350°C). [47]

4 Result and analysis

4.1 Physical characterization

Table 7 Summary of the investigated catalysts and abbreviation

Number	Sample	Notation
01	Iridium nanoparticle	Ir-nano benchmark
02	Iridium supported on ATO	Ir/ATO
03	Iridium supported on ATO(H_2O_2)	Ir/ATO_{H2O2} , H_2O_2 oxidized
04	Iridium vanadium supported on ATO	IrV/ATO
05	Iridium supported on Nb-doped SnO_2	Ir/NTO
06	Iridium Ruthenium catalyst	$Ir_{70}Ru_{30}$(70 wt% iridium)

To simplify the description of the investigated catalyst, I use the abbreviations shown above for the rest of this thesis.

Energy-dispersive X-ray spectroscopy

The physical characterization of IrV/ATO and Ir/ATO results are shown in the following graph.

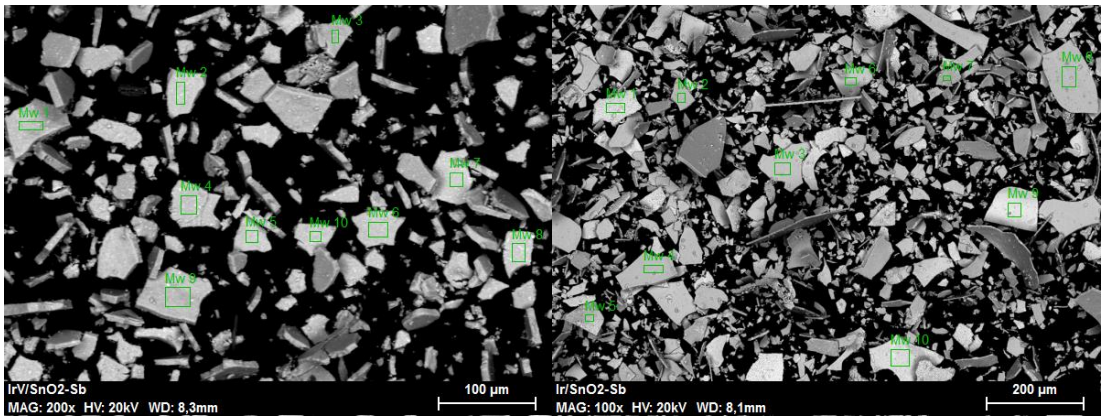

Figure 4-1 EDX image of IrV/ATO (left) and Ir/ATO (right) catalyst, for both of them 10 spots were selected for composition determination.

The data obtained by EDS analysis is given below with the unit of wt. %.

Table 8 Elemental analysis of IrV/ATO catalyst

Spectrum	O	Na	Cl	V	Sn	Sb	Ir
wt %							
Mw 1	15.59	0.82	0.32	3.14	39.62	4.29	27.48
Mw 2	12.5	0.51	0.46	3.22	44.56	5.17	26.5
Mw 3	15.98	0.88	0.35	2.9	39.52	4.01	27.31
Mw 4	7.11	0.85	0.57	3.74	46.25	6.5	30.72
Mw 5	10.18	1.2	0.46	3.32	45.87	5.58	27.64
Mw 6	11.57	0.91	0.49	3.14	44.38	5.52	26.28
Mw 7	13.49	1.25	0.32	3.72	41.04	4.42	28.41
Mw 8	6.88	0.81	0.45	3.62	44.28	6.41	32.84
Mw 9	17.01	0.91	0.27	3.1	39.04	3.97	26.62
Mw 10	11.3	0.95	0.41	3.22	45.29	5.16	26.26
Average	12.161	0.909	0.41	3.312	42.985	5.103	28.006
Standard deviation	3.50	0.21	0.09	0.29	2.85	0.92	2.16

Table 9 Elemental analysis of Ir/ATO catalyst

Spectrum	C	O	Na	Cl	Sn	Sb	Ir
wt %							
Mw 1	5.76	6.7	1.53	4.84	17.37	6.9	56.9
Mw 2	4.41	9.21	1.96	1.4	46.92	19.5	16.6
Mw 3	5.07	16.4	1.89	0.84	54.74	6.87	14.18
Mw 4	5.95	19.81	1.64	0.77	50.05	6.07	15.71
Mw 5	8.34	13.68	1.61	2.32	24.91	9.23	39.91
Mw 6	5.49	13.54	2.23	1.2	41.53	16.18	19.83
Mw 7	7.89	21.83	1.93	0.77	47.3	5.56	14.72
Mw 8	6.87	19.66	2.08	0.96	47.12	5.49	17.82
Mw 9	6.21	9.26	1.65	4.16	21.32	8.39	49.01
Mw 10	5	8.91	1.85	2.64	30.78	12	38.82
Average	6.099	13.9	1.837	1.99	38.204	9.619	28.35
Standard deviation	1.27	5.35	0.23	1.48	13.39	4.82	16.17

As one can see from Table 8 and Table 9, the average compositions of iridium for Ir/ATO and IrV/ATO are almost the same, both have the value of around 28 wt%. However, this value is a little bit lower than the stoichiometric value (30 wt%) calculated for supported catalyst synthesis, indicating that not all $IrCl_3$ was reduced after synthesis, although reductant $NaBH_4$ was added in excess. In addition, the error is inevitable since there are always noble metal losses in the cleaning procedure during synthesis.

Also, the theoretical weight ratio of vanadium to iridium should be 3:7 while actually most vanadium were missing or insoluble during synthesis. Besides, it is not hard to find that the iridium composition of Ir/ATO varied a lot among different areas indicating non uniform distribution of iridium on ATO support. On the contrary, iridium nanoparticles were well dispersed in IrV/ATO since the standard deviation of iridium composition in IrV/ATO is only 2.18 wt% compare to 16.18 wt% in Ir/ATO. Furthermore, about 5 wt% carbon was presented in both catalysts indicating CTAB surfactants were not fully removed after catalysts cleaning using ethanol and DI water for several times.

Scanning electron microscope

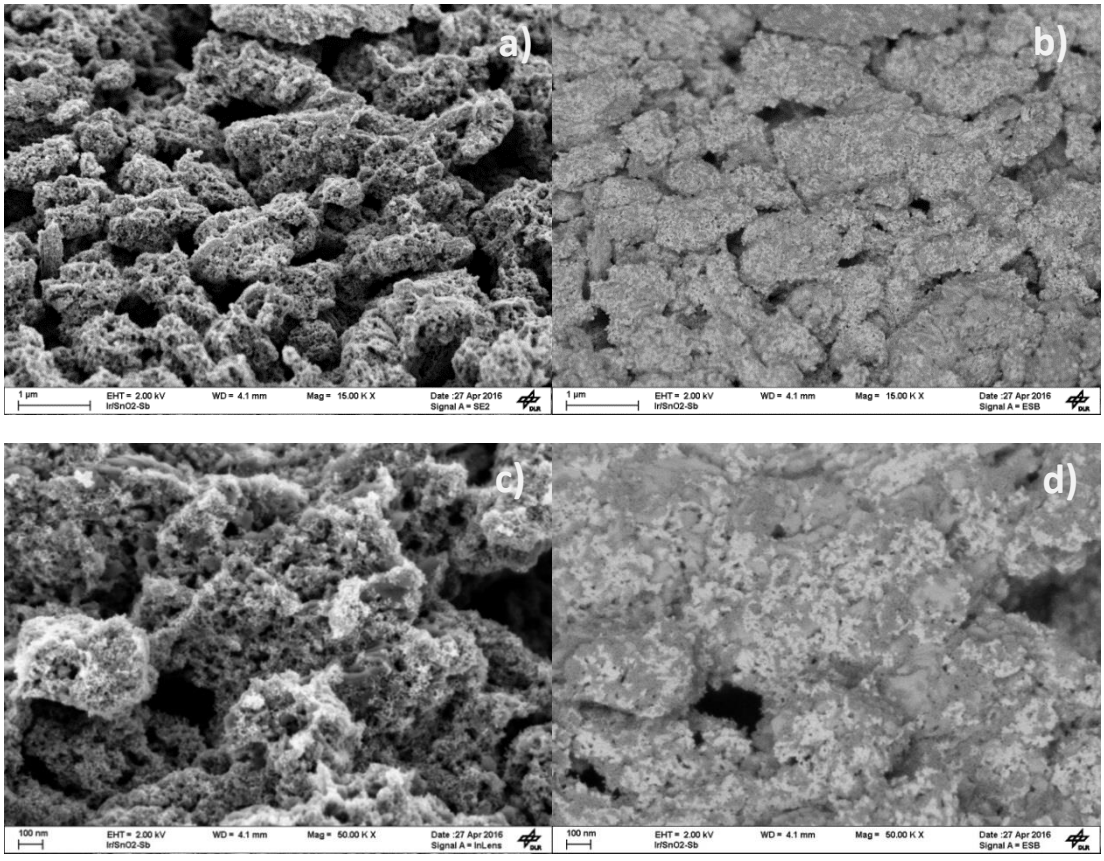

Figure 4-2 SEM images of Ir/ATO catalyst, Low (upper) and High (lower) magnification SEM iamges of Ir/ATO catalyst. Left side image acquired with secondary electron (SE) sensor and the right side image acquired from back-scattered electron (BSE or ESB) detector.

SEM images of Ir/ATO were recorded using secondary electron (SE) detector to get the morphology as well as energy selective backscattered (ESB) detector in order to get the enhanced compositional contrast image. The secondary electron images shows the morphology and the 3D structure of the material while the ESB images express the composition distribution of the catalyst material (bright site indicate the presence of metallic iridium, the darker site is the ATO support).

In Figure 4-2 (a) (c), one can observe in the SE images that Ir/ATO catalyst shows porous structure with a three dimensional network made up of interconnected particles. However, the pore size is unevenly distributed, in Figure 4-2 (d), some of the pore size of Ir/ATO is too large (microporous), which should be avoided to get a better Ir utilization. Regarding morphology, as illustrated in section 2.4, the catalyst supports with mesopores are preferable for OER catalyst since the optimum iridium particle size is in a range of a few nanometers.

Besides, in Figure 4-2 (b) (d), the surface of the Ir/ATO is pretty bright indicating that the surface of the support (ATO) is covered by iridium. However, the metallic iridium is not evenly dispersed on the ATO surface with some agglomeration.

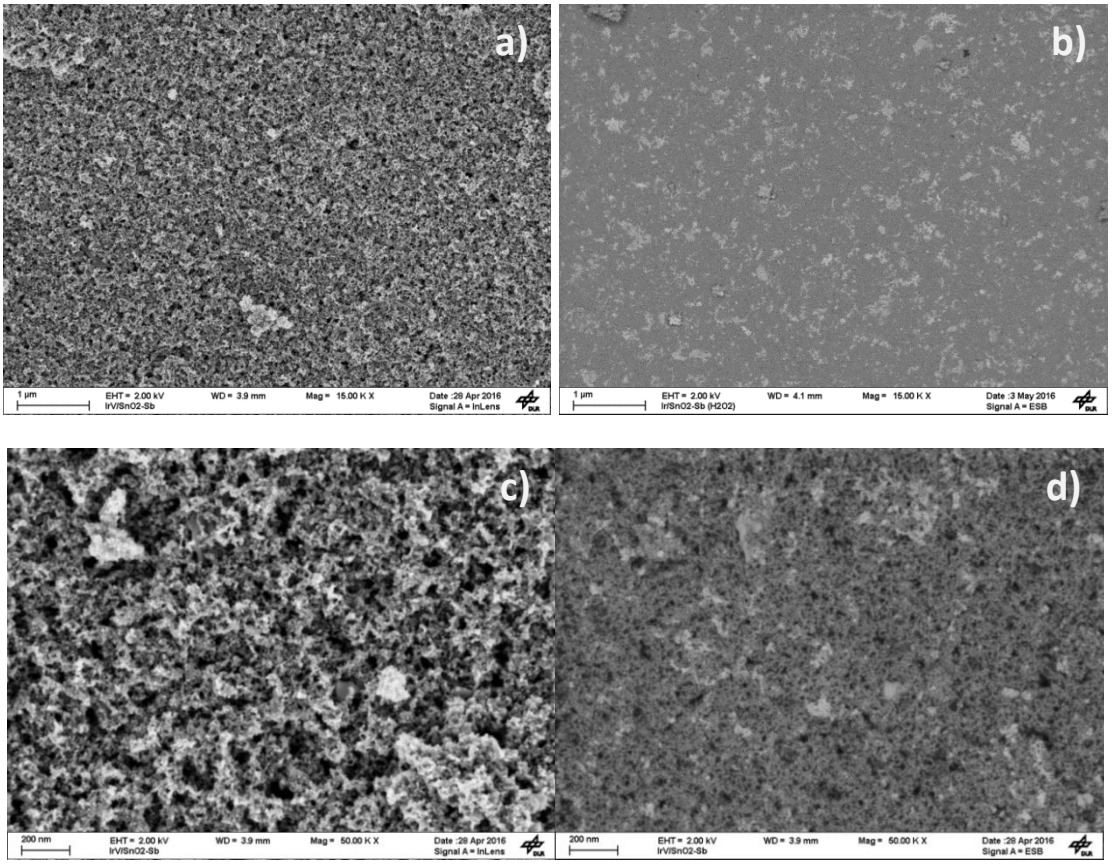

Figure 4-3 SEM images of IrV/ATO catalyst, Low (upper) and High (lower) magnification SEM iamges of Ir/ATO catalyst. Left side image acquired with Secondary electron sensor and the right side image acquired from back-scattered electron detector.

In Figure 4-3 (c), one can observe that IrV/ATO catalyst also shows porous structure with three dimensional network made up of interconnected particles. The pore size of IrV/ATO is much smaller compare to Ir/ATO with negligible micropores.

Besides, the surface of the IrV/ATO is also quite bright indicating that the surface of the support (ATO) is covered by iridium. Figure 4-3 presents fairly compact structure of IrV/ATO and iridium (bright dots) which seems to be scarce. The reason could be the dispersion of metallic Iridium into the porous structure of the ATO support and covered by the compact surface structure.

4.2 Electrochemical characterization of supported iridium catalyst

As described in section 2.4.1, the reference electrode is always located with a distance relative to the working electrode and introduces an uncompensated resistance (R_B). Therefore, EIS was used to determine the value of R_B as illustrated in section 2.4.3. The corresponding Bode plot and Nyquist plot for the thermostatic three-compartment glass cells were shown in the following graphs.

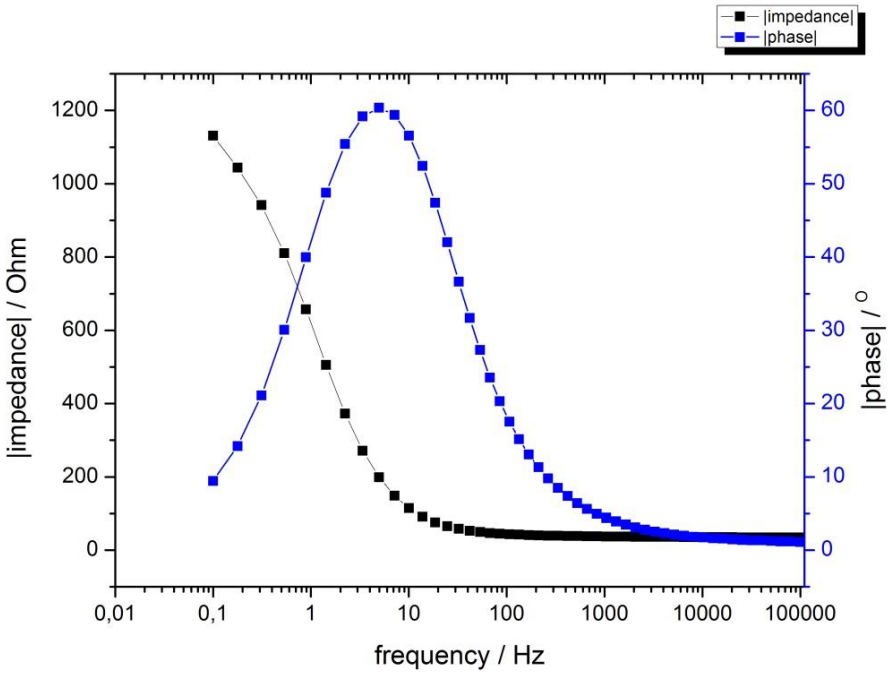

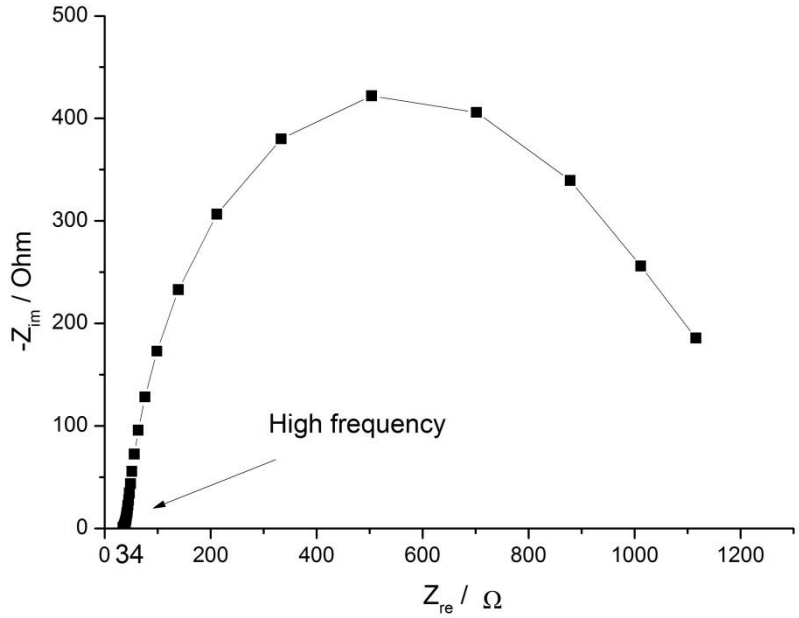

Figure 4-4 Bode plot (upper) and Nyquist plot (lower) of three-compartment glass cells (0.05M H_2SO_4, 25°C) for electrochemical characterization. The frequency range is from 100 mHz to 100 kHz, and the working electrode potential is 1.48V vs. RHE. The amplitude of the applied AC voltage is 10 mV.

From Nyquist plot, Figure 4-4 (b), at the highest frequency which is 100 kHz, we find that R_B is ca. 34 Ω. This resistance was then used in the following iR correction.

In order to compare all the catalysts, iridium nanoparticle (prepared using the protocol discussed in section 3.1.1) was set to be the benchmark and tested according to the test protocol shown in Table 5.

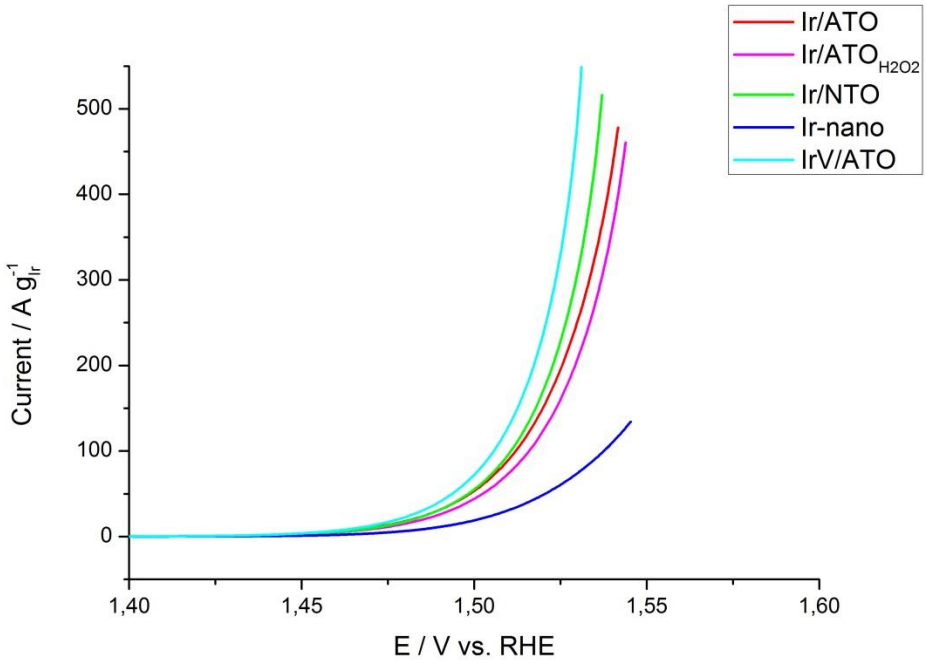

Figure 4-5 Steady-state polarization curves (iR corrected) for various supported catalysts and Ir-nano on GC-RDE electrode in 0.05M H_2SO_4 at 25°C. Potential sweep rate: 5mV s^{-1}.

Obviously, the mass OER activity for supported catalyst is much higher than Ir-nano benchmark, resulting from high active surface area and porous structure of the supported catalysts. The mass activity rose in the following order: Ir-nano ≪ Ir/ATO$_{H2O2}$ < Ir/ATO < Ir/NTO < IrV/ATO.

The mass activity or the current was calculated based on the theoretical iridium loading of 30 wt%. In fact, the actual iridium loading is about 28 wt% according to EDX analysis shown in section 4.1. Therefore, the mass activity for supported catalyst is actually higher than the presented value.

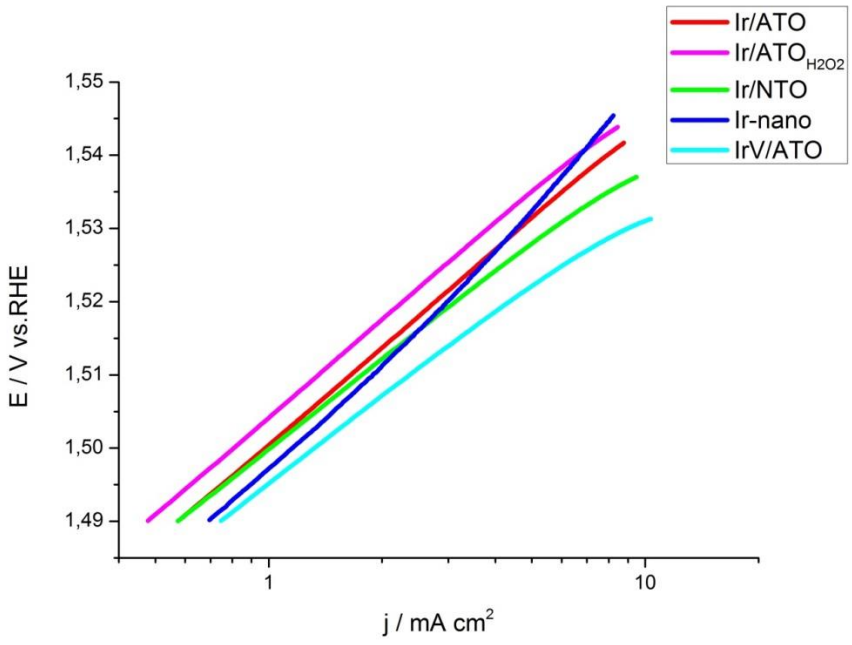

Figure 4-6 Tafel plot for various supported catalysts and Ir-nano on GC-RDE electrode in 0.05M H_2SO^4 at 25°C. Potential sweep rate: 5mV s^{-1}.

Tafel plot, especially Tafel slope is an important kinetic parameter to evaluate the OER activity of the support as well as the changes of the reaction mechanism during the OER. As previously reported [48,49], the Tafel slope in the range of 40 to 60 mV dec^{-1} is common for iridium oxide. From Figure 4-6, we can find that introducing support materials causes a decrease in Tafel slope which leads to an increase of the OER activity. Again, IrV/ATO outperformed Ir-nano benchmark and other supported catalysts.

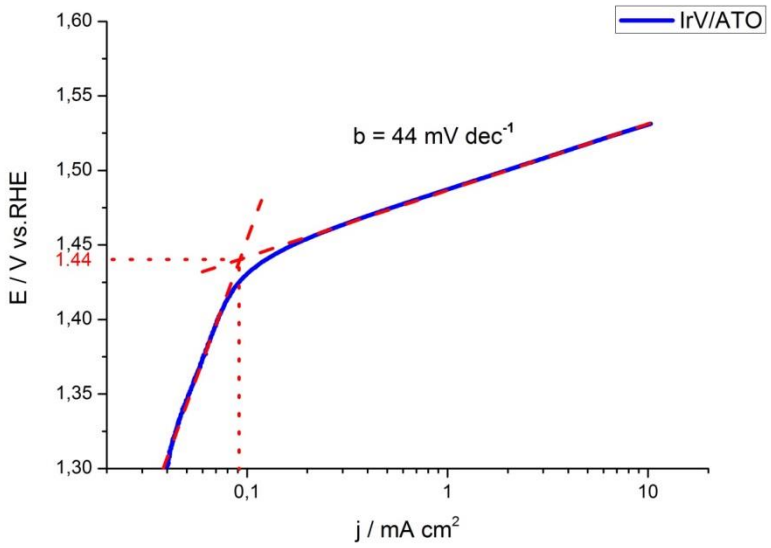

Figure 4-7 iR corrected Tafel plot of IrV/ATO catalyst.

The upper graph shows the Tafel plot of IrV/ATO catalyst which has the best performance among all. The onset potential for OER was found at the intersection of the two lines, which is equal to 1.44 V vs. RHE. Also, the onset potential for Ir/ATO and Ir-nano all have the similar value of about 1.44V vs. RHE which corresponding to over-potential η = 210mV, as shown in Table 10.

Table 10 Tafel slope comparation of different supported catalysts (25°C)

#	Sample	Tafel slope b	Onset potential
01	Ir/ATO	50 mV/dec	1.43 V
02	Ir/ATO_{H2O2}	51 mV/dec	1.43 V
03	IrV/ATO	44 mV/dec	1.44 V
04	Ir/NTO	45 mV/dec	1.44 V
05	Ir-nano	55 mV/dec	1.43 V

The Tafel slope b of 44-55mV/dec suggested that at high current density the rate determining step is the second step of deprotonation of the absorbent (2b) in Table 1. And the onset potential for OER is almost the same for all supported catalysts and Ir-nano benchmark catalyst indicating the reaction mechanism is similar for all Ir-based catalysts.

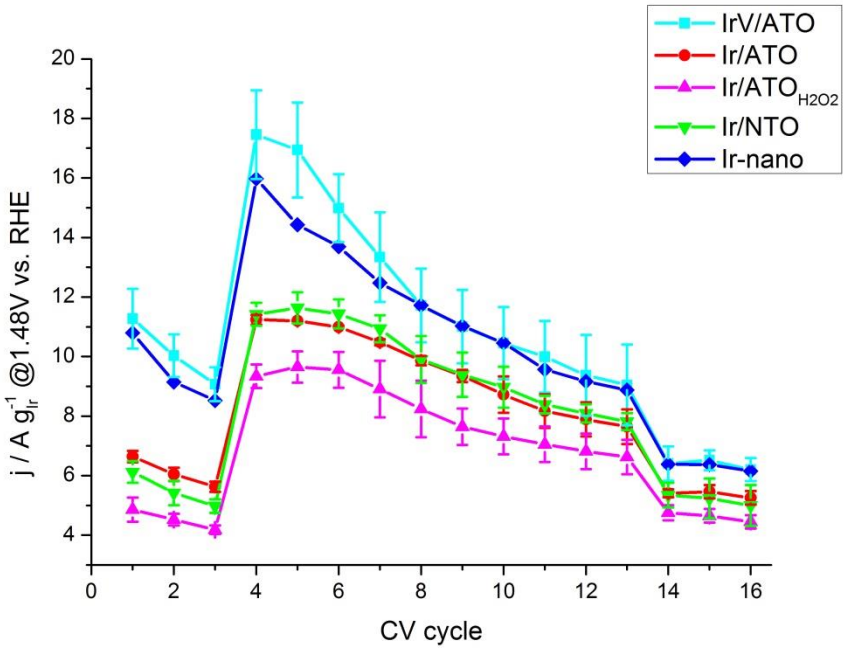

Figure 4-8 mass-normalized OER activity (at 1.48 V vs. RHE) vs. CV cycle number for various supported catalysts and Ir-nano catalyst in 0.05M H_2SO_4 at 25°C. Potential sweep rate: 5mV s^{-1}.

The graph is the OER activity overview among all supported catalysts and one unsupported catalyst @1.48V vs. RHE and their short-time stability demonstration. From which we can see, IrV/ATO catalyst shows the highest OER activity among all the investigated supported catalysts. Ir/SnO_2-Sb and Ir/SnO_2-Nb shows the similar OER activity even though different support material was used. Ir/ATO_{H2O2}, which means Ir/ATO oxidized by H_2O_2, shows a slightly lower OER activity compare to Ir/ATO and Ir/NTO. Since the first three cycles and last three cycles use $5mVs^{-1}$ and the 10 CV cycle in the middle used 20 mV s^{-1}, the current seems to increase dramatically because of high capacitive behavior of the catalyst and solution interphase.

Through comparing IrV/ATO with the Ir-nano benchmark catalyst, as can be seen, the mass activity of IrV/ATO is approximately 4 times higher than Ir-nano benchmark catalyst before EC oxidation protocol (Seq. No2 in Table 5) and 3.5 times higher after EC oxidation protocol. In fact, the actual mass activity of IrV/ATO should be higher because the actual iridium loading should be smaller than 30 wt% due to losses in synthesis cleaning process. After EC oxidation protocol, the mass activity decreased because the initial high current (before EC oxidation protocol) can be contributed by iridium oxidation as well as impurities oxidation, which disappeared after EC oxidation protocol (iridium may irreversibly oxidized (e.g. Ir (IV) to Ir (V))[50] as mentioned in section 3.2.3.

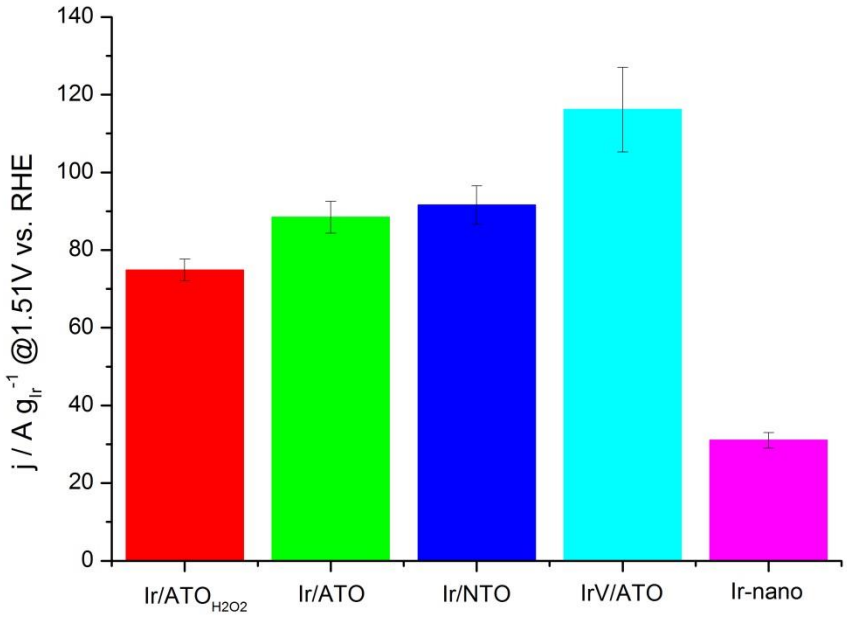

Figure 4-9 Iridium-mass-normalized activity of all the supported catalysts and Ir-nano benchmark @1.51 V vs. RHE.

Since comparing OER activity under overpotential of 280 mV has been well accepted in the community, we compare the mass-normalized activities at 1.51 V vs. RHE of all four supported catalysts and Ir-nano benchmark catalyst. As illustrated in Figure 4-4, Ir/ATO$_{H2O2}$ and Ir/NTO and Ir/ATO electrocatalysts exhibited a threefold higher mass activity compared to the Ir-nano benchmark, while IrV/ATO showed almost fourfold higher activity compared to Ir-nano benchmark. The much larger OER acitivty comes from the high specific surface area of the support, homogeneous dispersion of iridium metal on the surface support material and appropriate pore size of the support material as illustrated in section 2.4. These excellent mass-normalized activity of the supported iridium catalysts may due to i) high iridium utilization since Ir nano-particles were well dispersed on the substrate materials ii) improved mass transportation, either water transportation or oxygen bubbles detachment, on the porous aerogel substrate surface. [51,50]

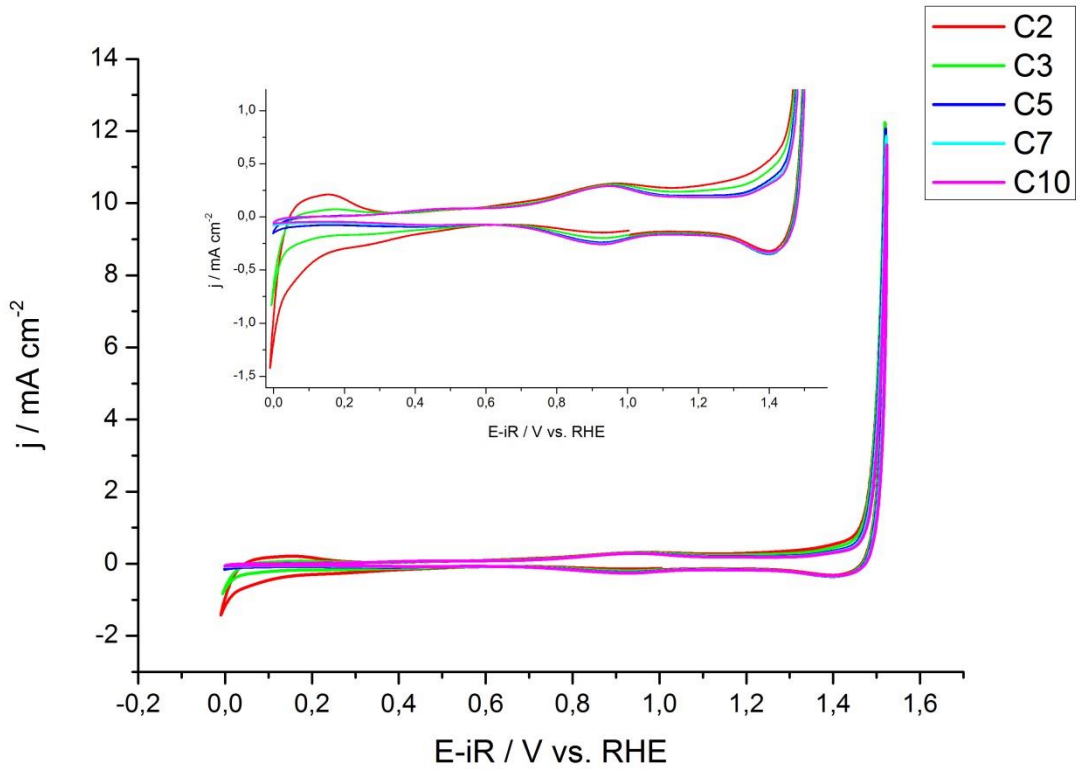

Figure 4-10 Cyclic voltammogram of IrV/ATO measured in N_2 saturated 0.05M H_2SO_4 with different scan number (e.g. C1 means the first cycle), the starting potential was 0.7 V vs. RHE. Measurements were carried out with sweep rate of 20 mV s^{-1} at 25°C.

In general, the solid-state redox transitions of noble metal oxide usually accompanied with ion exchange processes in the form of redox waves across the corresponding potential window.[49, 52] As for iridium oxide, the redox process could be described by the equation below:

$$IrO_x(OH)_y + \delta H_{(solution)}{}^{+} + \delta e_{oxide}{}^{-} \rightarrow IrO_{x-\delta}(OH)_{y+\delta}$$

To evaluate the electrochemical properties of the IrV/ATO catalyst, CV were performed in 0.05M H_2SO_4 solution with the sweep rate of 20 mV s^{-1}, the IrV/ATO catalyst was selected to illustrate the electrochemical process during CV. As can be seen, the adsorption of hydrogen took place at the potential window between ca. 0V to 0.35V vs. RHE. The upper limit 0.35V of the adsorption process was related to the hydrogen under-potential deposition (UPD) on metallic iridium surface.[11] However, the metallic iridium on the surface gradually oxidized to iridium oxide species through potential cycles between 0 V and 1.6 V vs. RHE. In particular, metallic iridium was first oxidized to Ir (III) at potential window of 0.4 V to 0.8 V vs. RHE. Because of that, the maximum cathodic current peaks which results from the hydrogen under-

potential deposition gradually decreased and disappeared completely after 5 cycles. As can be seen, in the potential window between 0.45 and 0.55V vs. RHE corresponds to the double layer charging process. Besides, in potential region of 0.8 V to 1.2 V vs. RHE, the anodic and cathodic peaks, shown in the insert of Figure 4-6, were attributed to Ir (III) oxide to Ir (IV) oxide transition. [53]

Furthermore, the electrochemical process occurred in potential between 1.2 to 1.5 V vs. RHE was most likely attributed to irreversible oxidation of Ir (IV) to Ir (V) as shown in Figure 4-6. [53]. Based on above mechanism, we could make an assumption that the IrV/ATO catalyst was irreversibly converted to hydrous iridium oxide species (IrO_x) with simultaneously loss of the metallic character.

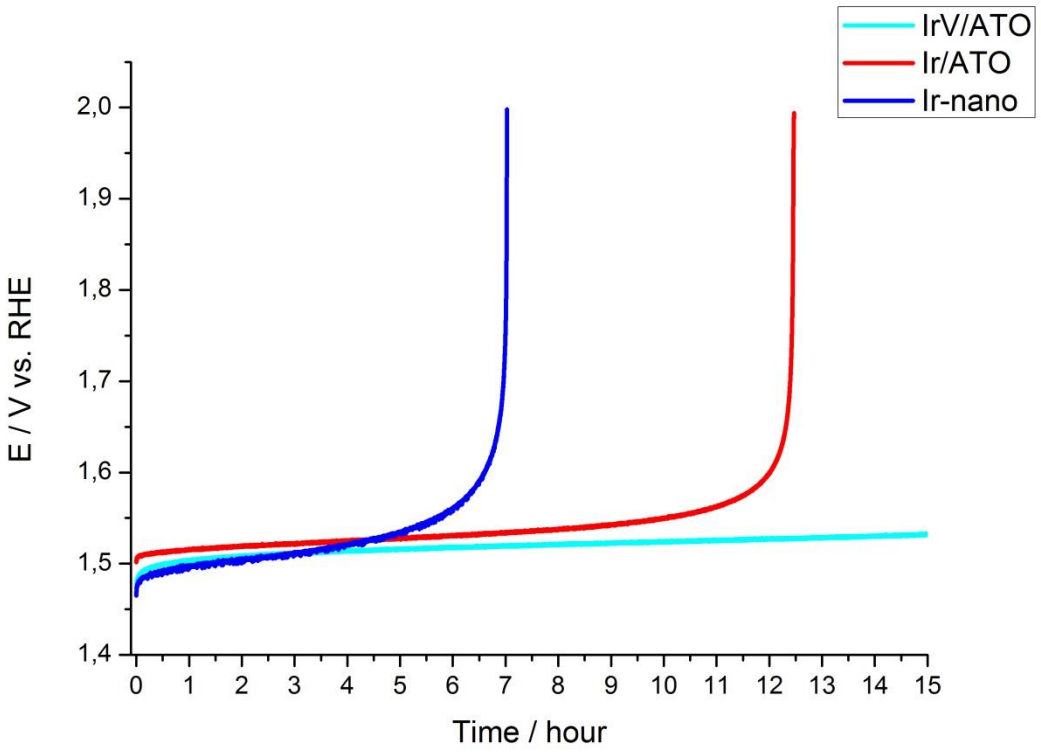

Figure 4-11 Stability test of IrV/ATO, Ir/ATO, Ir nano for 20 hours at constant current mode (1 mA/cm^2), reaction conditions: N^2 purged, catalysts loading **12 µg** with the GC-RDE area of 0.196 cm^2, 1600 rpm.

All the recorded potential gradually increased during stability test, indicating a certain degree of instability due to corrosion, particle agglomeration or catalyst dropping from the electrode surface. Those explanations were only hypothesis since the catalyst could not be collected after the stability test (stuck on the surface of the GC-RDE), thus could not be used for any

further physical characterizations. The electrochemical stability of IrV/ATO, Ir/ATO along with the benchmark Ir-nano catalyst was tested under constant current load conditions (chronopotentiometry) for the duration of 15 hours (Figure 4-13). The working electrode potential increased gradually for Ir/ATO and Ir-nano catalysts elucidating the degradation of the catalysts.

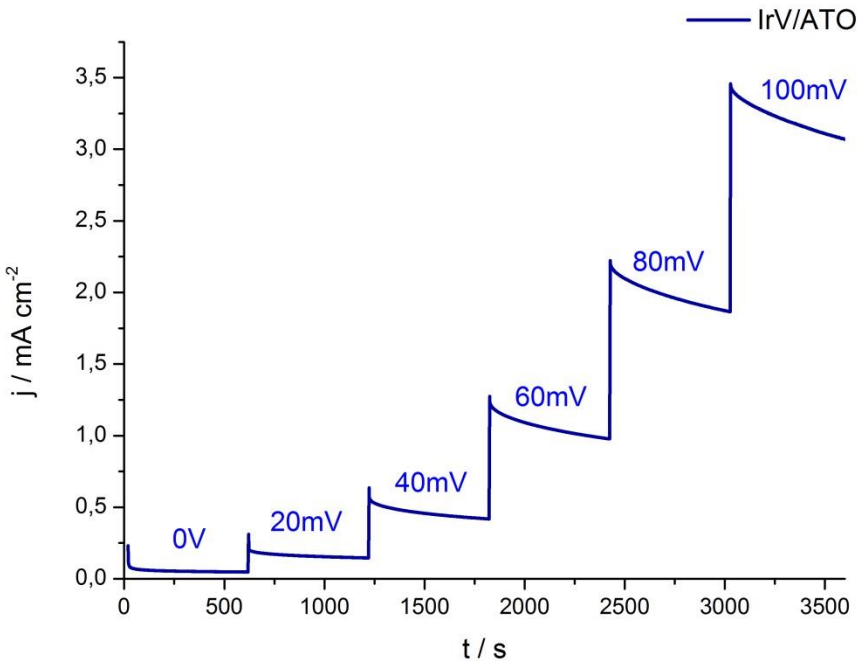

Figure 4-12 Duty cycle protocol (using the first Duty cycle test of IrV/ATO as an example), 10 minutes potential steps from η = 0 V to 100 mV at 1600 rpm in N_2-saturated 0.05M H_2SO_4.

As shown in Figure 4-12, we can see that the current decreased gradually during one duty cycle for each potential step indicating the short time degradation of the catalyst as well as the capacitive behavior of the electrode. After the stability test, the OER activity was measured and the results are presented in Figure 4-13.

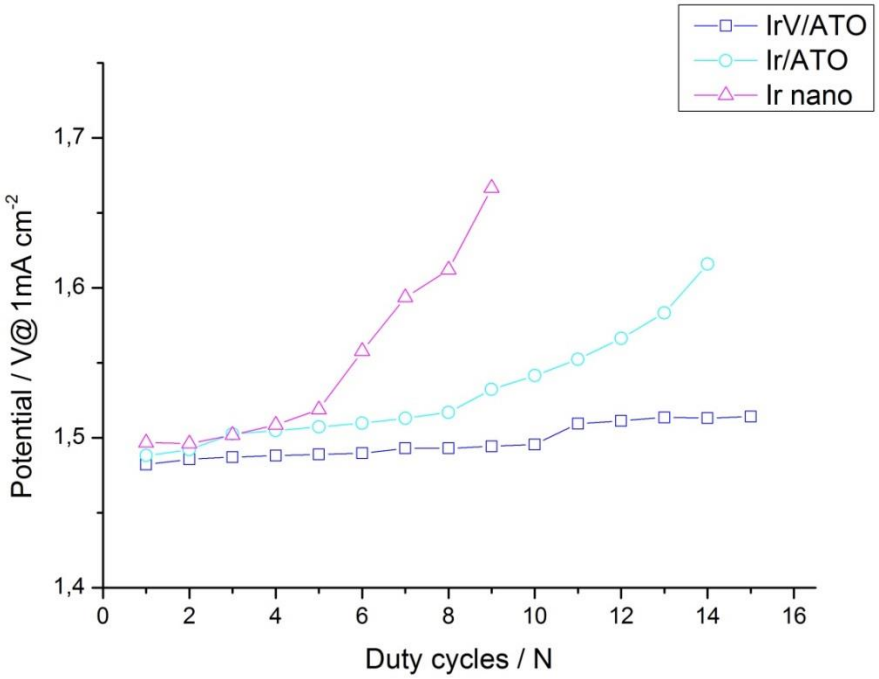

Figure 4-13 Potential at 1 mA cm^{-2} using Cyclic voltammetry protocol illustrated in Fig 3-5 (range: 1 V to 1.6 V, sweep rate: 5mV s^{-1}, two scans) after Duty cycle of IrV/ATO Ir/ATO and Ir-nano. Reaction conditions: N2 purged, catalysts loading **12 µg** on the GC-RDE area of 0.196 cm^2, 1600 rpm.

As described before, the stair-case duty cycle test protocol was much harsher than 15 hours stability test protocol. The Ir/ATO and Ir nano catalysts were degradated after 4th and 8th duty cycle, respectively. Again, the most stable catalyst was the IrV/ATO, which showed great stability in the duty cycle test. Even after 15 duty cycle, the potential at 1mA cm^{-2} of the second CV scan after duty cycle increased only 0.28 V comparing that of first duty cycle.

Another thing that has to be considered was the support degradation at high potential region. Thus we used the CV protocol (Sequence 1 and 2) described in Table 4 to find out how ATO performed in such harsh conditions. ATO ink was prepared using the same protocol described in section 3.2.1 and coated on the RDE surface.

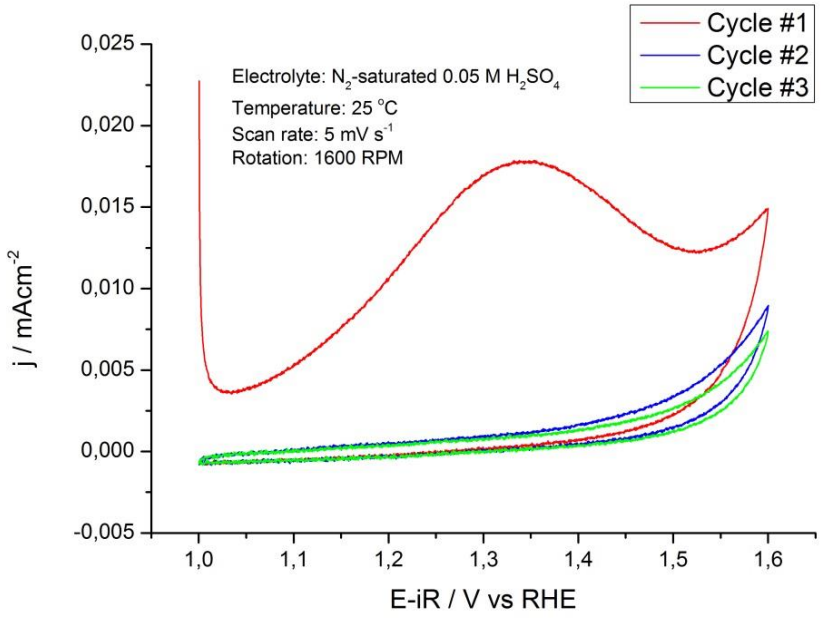

Figure 4-14 Cyclic voltammogram of ATO support from 1.0 V to 1.6 V, scan rate: 5 mV s^{-1}

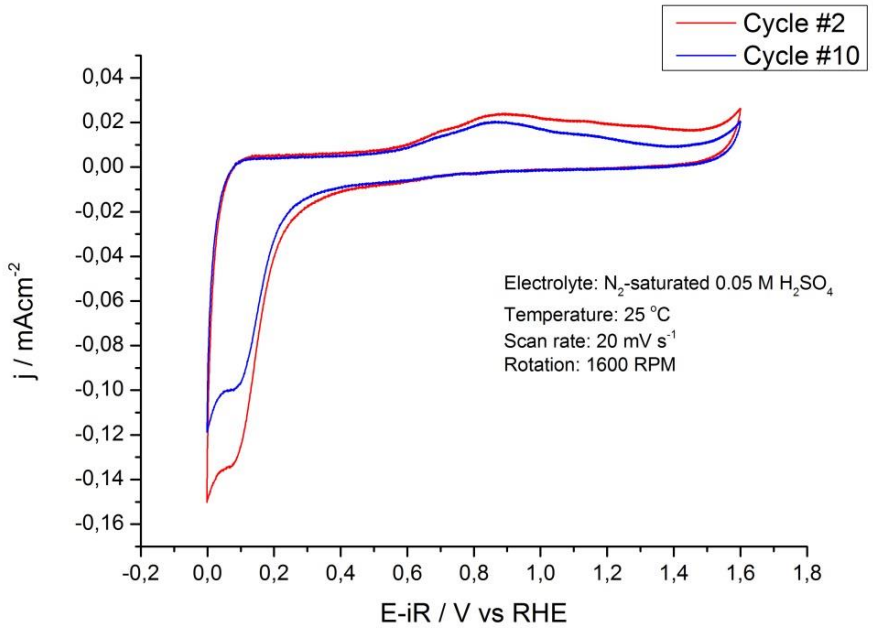

Figure 4-15 Cyclic voltammogram of ATO support from 0 V to 1.6 V, scan rate: 20 mV s^{-1}

The OER activity test for pure ATO without noble metal loading revealed that the ATO support was not absolutely stable at high potential (>1 V) and after 1 cycle the current dropped significantly indicated that the support material may went through irreversible oxidation process. Furthermore, the negative current density at around 0V vs. RHE in Figure 4-15 may indicate that hydrogen adsorption occurred on the ATO surface.

4.3 Copper under-potential deposition

The potential limits used to get the cyclic voltammogram for iridium-based catalyst in both background cell and working cell (Cu-containing), are from 0.2 V to 0.72 V vs. RHE. Both the copper under-potential deposition and over-potential deposition are observed within this potential window as shown in Figure 4-16. As described before, the under-potential deposition corresponds to the monolayer deposition of copper onto metallic iridium, while over-potential deposition relates to the growth of copper bulk over-layers.

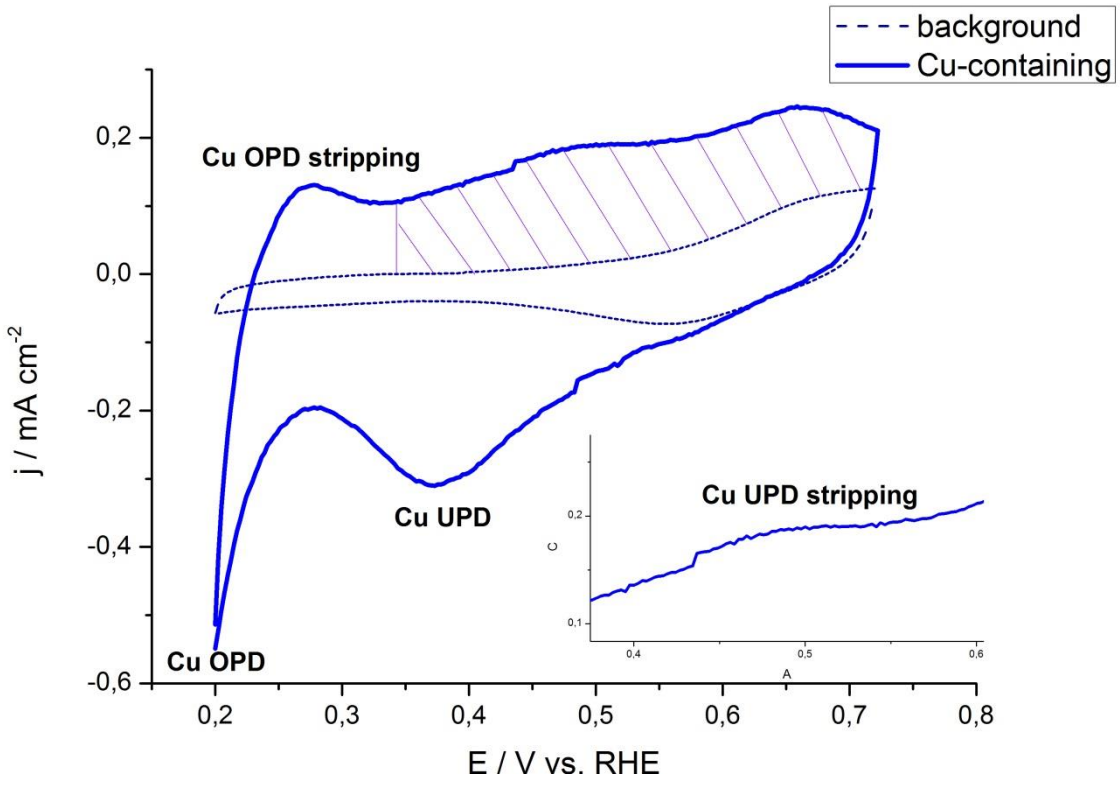

Figure 4-16 Second Cyclic voltammogram of Ir/ATO in 0.5M H_2SO_4 (background) and 5mM $CuSO_4$ + 0.5M H_2SO_4 (Cu-containing) electrolyte. Scan rate: 20 mV s^{-1}, N_2 (background) and Ar (Cu-containing) saturated.

In figure 4-16, the second CV scan of Ir/ATO catalyst was presented, from which we can clearly identify the peaks of Cu UPD, OPD and Cu OPD stripping (Cu UPD stripping in the insert).

The dash line represents the electrode CV behavior in the background electrolyte which is 0.5M H_2SO_4. It is not hard to notice the presence of a reversible anodic peak in the potential window between 0.6 - 0.8 V vs. RHE, which corresponding to iridium oxide species on the surface of the catalyst. Also, the double layer charging current is clearly represented in the potential window from 0.2 V to 0.4 V vs. RHE.

The solid line is the CV curve obtained in the Cu-containing electrolyte. The CV scans started at 0.2 V vs. RHE and firstly moved toward the positive potential where the Cu OPD stripping peak was found between 0.23 V to 0.3 V vs. RHE with peak potential value of E_{p1} = 0.275 V vs. RHE. And the over-potential deposited Cu was completely removed at 0.35 V vs. RHE. Cu UPD stripping was started right after the Cu OPD stripping at potential 0.35 V vs. RHE and continued to strip in a broad potential range as can be seen in the insert of Figure 4-13. However, the insert does not present a well-defined Cu UPD stripping peak which has a light peak of E_{p2} = 0.485 V vs. RHE.

During the cathodic scan, the Cu UPD was first observed at potential between 0.3 V and 0.6 V vs. RHE with a broad peak and the peak value of E_{upd} = 0.37 V vs. RHE. As the cathodic scan proceeded, the subsequent Cu OPD multilayer started to deposit and could deposit for a large amount if the scan went to a more negative potentials.

It was previously reported that the under-potential shift ($\Delta E_p = E_{UPD} - E_{OPD}$) corresponded to the difference of binding energy between a metal adatom to a foreign substrate and the metal adatom to its own bulk lattice.

Based on the peak value of Cu OPD stripping and Cu UPD stripping obtained from Figure 4-13, ΔE_p could be calculated:

$$\Delta E_p = E_{UPD} - E_{OPD} = E_{p2} - E_{p1} = 0.485\ V - 0.275\ V = 0.21\ V$$

Thus, the difference of Gibbs free energy is therefore:

$$\Delta G = nF\Delta E_p = 2 * F * \Delta E_p = 40.5\ kJ \cdot mol^{-1}$$

Where F stands for the Faraday constant and n is the electron transfer of Copper deposition, which is denoted in section 3.3. Therefore, the UPD Cu monolayer deposition is more stable than subsequent Cu over-layers deposit by 40.5 $kJ \cdot mol^{-1}$. This value is larger than the published value for Cu deposition on Ruthenium. [54]

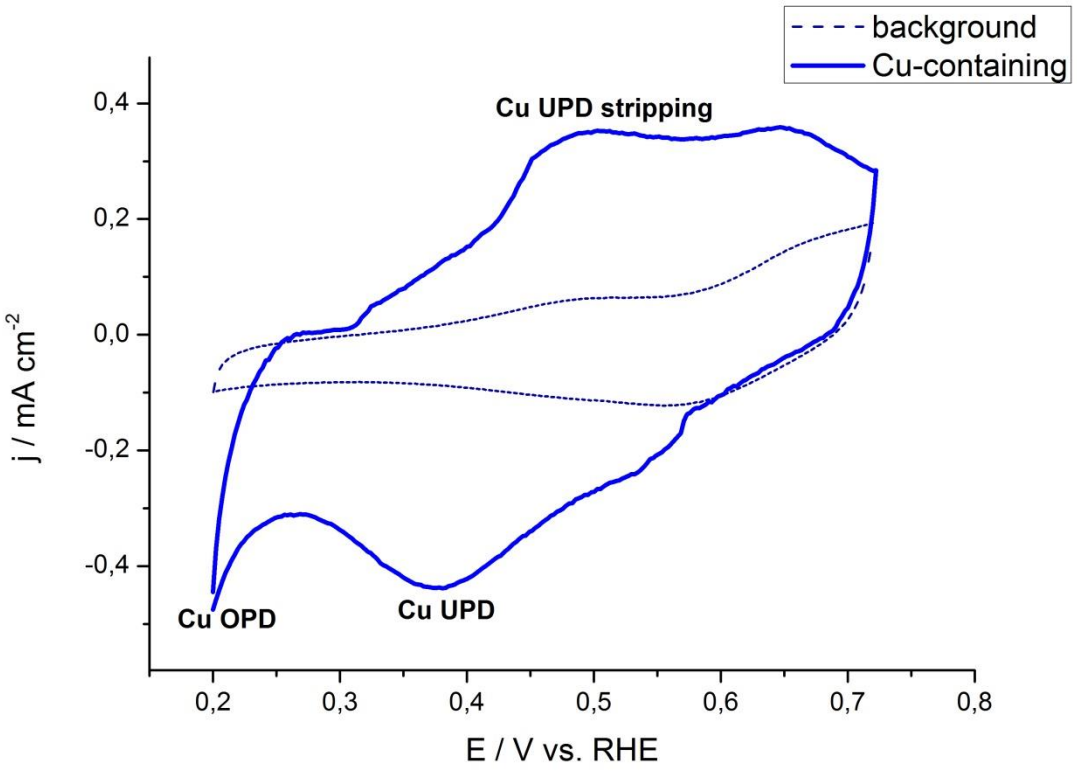

Figure 4-17 Second Cyclic voltammogram of IrV/ATO in 0.5M H_2SO_4 (background) and 5mM $CuSO_4$ + 0.5M H_2SO_4 (Cu-containing) electrolyte. Scan rate: 20 mV s^{-1}. N_2 (background) and Ar (Cu-containing) saturated.

In Figure 4-17, the CV of IrV/ATO catalyst shows similar shape as Ir/ATO catalyst. Cu UPD was found at potential between 0.26 V to 0.48V vs. RHE with the peak value of E_{upd} = 0.375 V vs. RHE. Also, Cu UPD peak potential of IrV/ATO is almost the same as that of Ir/ATO. If we compare the Cu UPD peak of IrV/ATO and Ir/ATO, IrV/ATO presents a much larger current density and a broader peak than Ir/ATO indicating that there are more Cu atoms deposited on IrV/ATO surface. As the potential went toward more negative value, Cu OPD started to take place. And the Cu OPD of IrV/ATO has a smaller peak than Ir/ATO. As a result, the Cu OPD stripping peak for IrV/ATO is less obvious compare to Ir/ATO. On the contrary, the Cu UPD stripping of IrV/ATO presents a much larger peak than Ir/ATO, which again confirms that there is more Cu deposited on IrV/ATO. The UPD stripping peak of IrV/ATO is found to be E_p = 0.5 V vs. RHE and much similar to that of Ir/ATO.

Unexpectedly, the background CV of IrV/ATO shows the similar shape as Ir/ATO but higher current density (with same amount of iridium loading), resulting in a second peak at 0.65 V vs. RHE in the anodic scan.

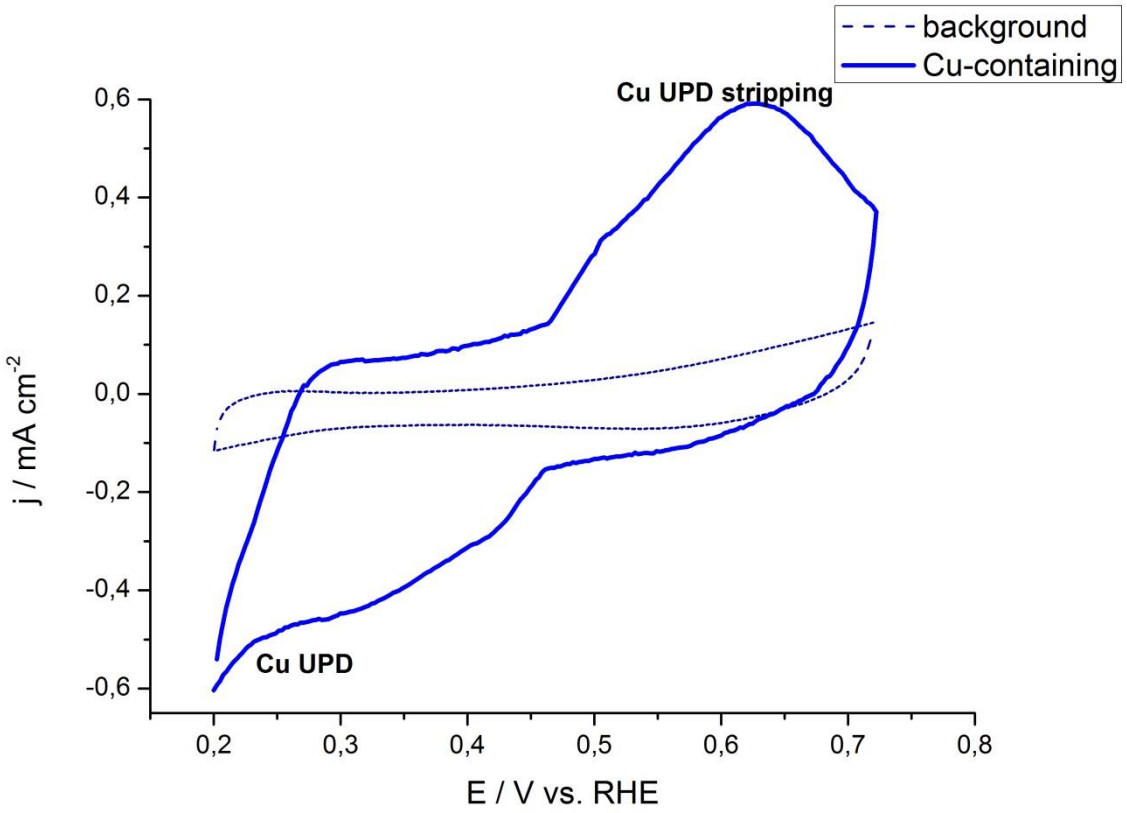

Figure 4-18 Second Scan Cyclic voltammogram of Ir-nano in 0.5M H_2SO_4 (background) and 5mM $CuSO_4$ + 0.5M H_2SO_4 (Cu-containing) electrolyte. Scan rate: 20 mV s^{-1}, N_2 (background) and Ar (Cu-containing) saturated.

In order to explain the mechanism of Cu UPD, as shown in Figure 4-18, the CV of Ir-nano was measured using exactly the same experiment condition. One can notice that there is no Cu OPD or OPD stripping takes place. Instead, it shows much broader UPD and UPD stripping peaks, because it has larger iridium loading compared with supported iridium catalysts, therefore more surface active sites for Cu to deposit on. Moreover, not all the metallic iridium was "occupied" by Cu with the adsorption ratio of one Copper atom to one surface iridium atom, since there is no peaks for Cu OPD and the current was still increasing as the potential went to the lower limit.

Finally, the charge associate with the Cu UPD stripping and deposition, corrected for the background, were found by integrating the shadow area (e.g. in Figure 4-16) and then divided by the scan rate.

$$Charge\ \ [C] = \frac{integrated\ area\ \ [V \cdot I]}{scan\ rate\ \ [V\ s^{-1}]}$$

The voltage range used in integration is from 0.35 V to 0.72 V where Cu UPD stripping takes place. The specific area charge corresponding to Cu UPD stripping for Ir/ATO, IrV/ATO, Ir/NTO, Ir/ATO_{H2O2} and Ir-nano benchmark catalyst were calculated using the above equation. The surface area of the electrode is 0.196 cm^{-2}. Result is then presented in Figure 4-19.

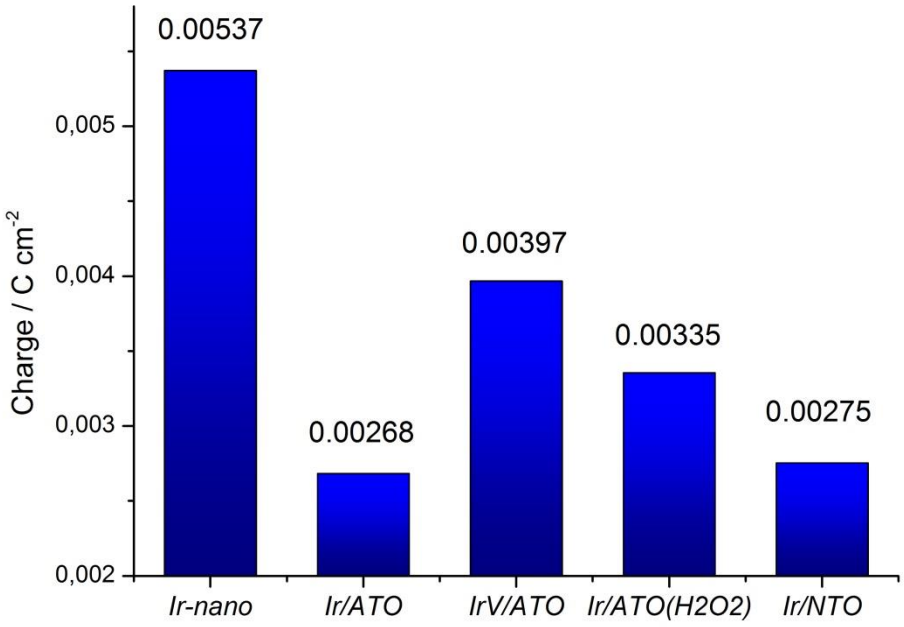

Figure 4-19 Comparison of Charge associated with Cu UPD for different catalysts.

As can be seen in Figure 4-19, Ir-nano benchmark catalyst shows the highest Cu UPD Stripping charge, which is not surprising since Ir-nano has the highest iridium loading. Among the four supported catalysts, IrV/ATO outperformed the other three catalysts indicating that it has the highest surface active sites. Surprisingly, Ir/ATO_{H2O2} also shows pretty large Cu UPD stripping charge, resulting from its compact surface structure with ideal pore size similar to IrV/ATO (see Appendix SEM).

Assuming that the copper deposited in the Cu UPD region corresponds to monolayer coverage of Copper atoms and one copper atom adsorbed on one surface iridium atom, the number of iridium on the surface of each catalyst could be calculated using the following formula assuming two electron transfer for the Cu UPD as discussed in section 3.2.5.

$$number\ of\ Iridium\ \ [cm^{-2}] = \frac{Charge\ \ [C \cdot cm^{-2}]}{2e\ [C]}$$

Where e is the elementary charge of an electron, the result is shown in Table 11.

Tabel 11 Surface iridium sites for Cu UPD, unit: cm^{-2}

Ir-nano	Ir/ATO	IrV/ATO	Ir/ATO_{H2O2}	Ir/NTO
1.68×10^{16}	8.4×10^{15}	1.24×10^{16}	1.05×10^{16}	8.6×10^{15}

4.4 Electrochemical characterization of bimetallic IrRu catalysts

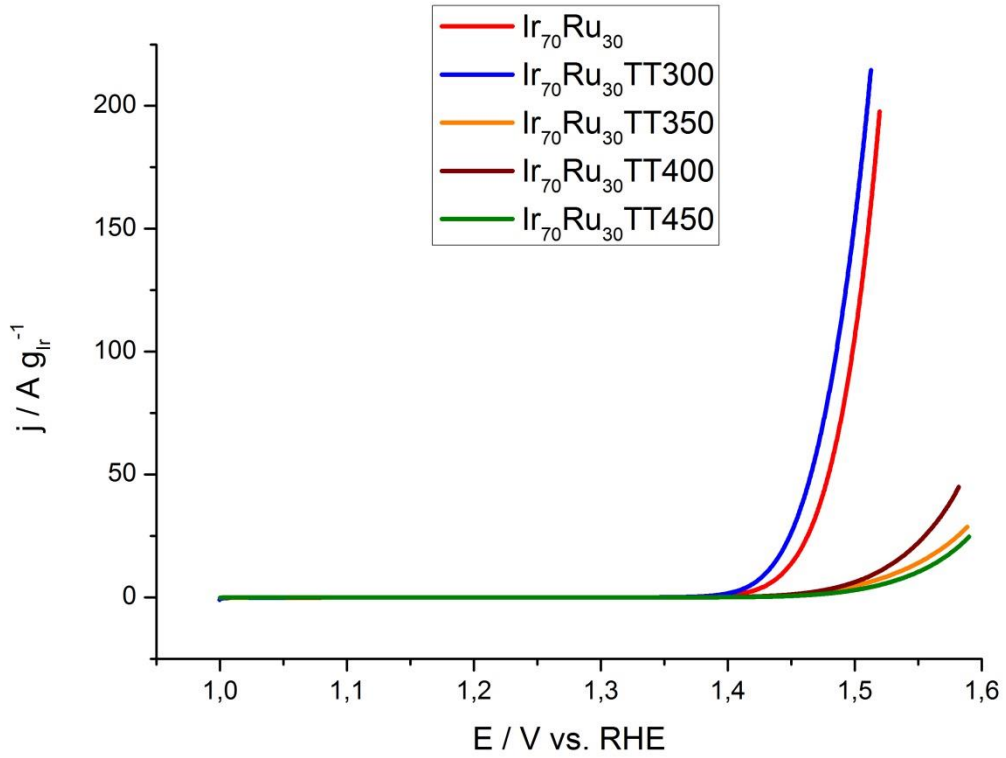

Figure 4-20 Steady-state polarization curves (iR corrected) for $Ir_{70}Ru_{30}$ and different thermally treated $Ir_{70}Ru_{30}$ (300°C, 350°C, 400°C, 450°C) in N_2-satuated 0.05M H_2SO_4, scan rate: 20 mV s^{-1}, rotation speed: 1600 rpm. TT300 stands for thermally treated at 300°C for half hour and others are similar.

Obviously, as-prepared $Ir_{70}Ru_{30}$ and $Ir_{70}Ru_{30}$TT300 express much higher OER mass activity at 1.48 V vs. RHE ($\eta = 250\,mV$) comparing to the other thermally treated catalysts. Besides, $Ir_{70}Ru_{30}$TT300 has a better OER mass activity compared to as prepared $Ir_{70}Ru_{30}$. In summary, the OER mass activity rose in the follow order: $Ir_{70}Ru_{30}$TT450 < $Ir_{70}Ru_{30}$TT350 < $Ir_{70}Ru_{30}$TT400 ≪ $Ir_{70}Ru_{30}$ < $Ir_{70}Ru_{30}$TT300. The OER activity decreased with increasing temperature, except for $Ir_{70}Ru_{30}$TT400 with slight increase, which may due to the decrease of the ohmic resistance with increasing annealing temperature.[55] One possible explanation could be impurities, since impurities disappeared during anneal process. Another and much possible reason is that annealing leads to particle growth and a much smaller electrochemical active surface area.[56]

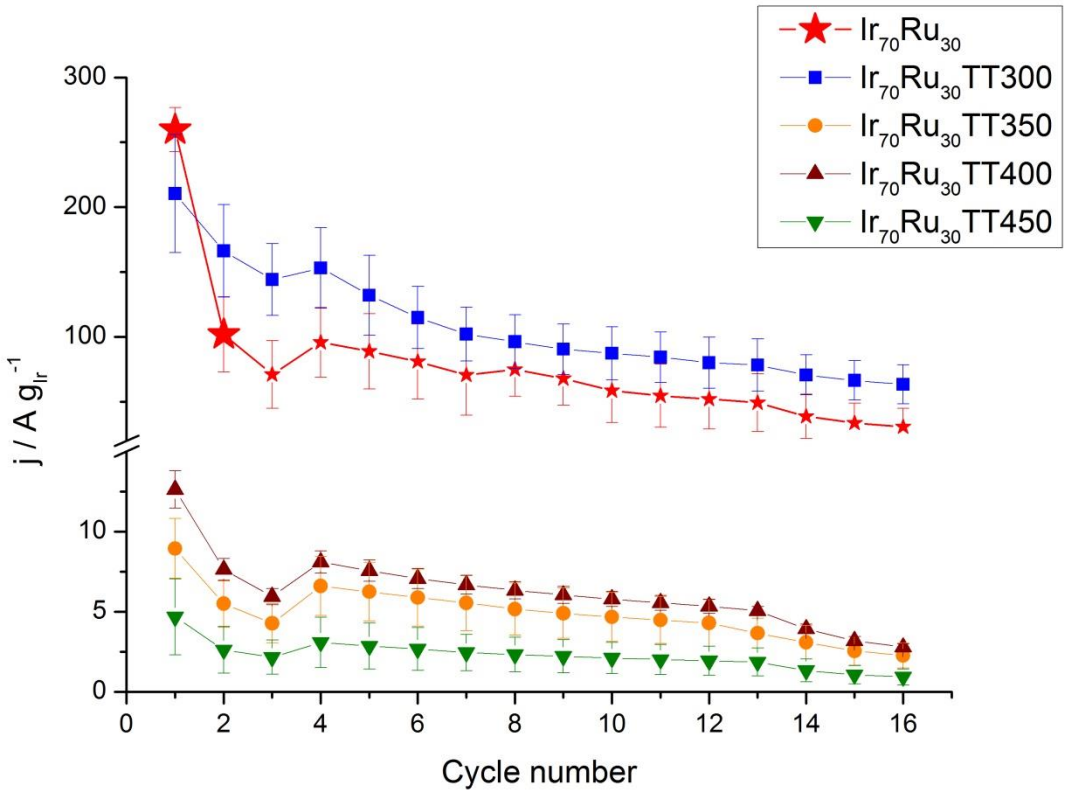

Figure 4-21 OER mass activity comparison (@ 1.48 V vs. RHE) of different thermal treatment (300°C, 350°C, 400°C, 450°C) and as prepared $Ir_{70}Ru_{30}$ catalysts. Experiment duration: approximately 1 hour.

In Figure 4-21, as for $Ir_{70}Ru_{30}$TT300, it is obvious that the OER mass activity decreased dramatically after the first CV cycle while the OER mass activity remain relatively high after

three CV cycles, indicating an improved catalyst stability towards OER after annealing at 300°C for half hour. As mention in section 3.2.6, ruthenium is thermodynamically favored to be oxidized to RuO_4 during OER activity test, which serve as a corrosion product on the electrode surface and then dissolve into the electrolyte. And as mention in section 3.2.6, Ru had already oxidized to its crystalline phase at 300°C (and would not dissolve into the electrolyte). Therefore, $Ir_{70}Ru_{30}$TT300's OER activity did not drop dramatically as $Ir_{70}Ru_{30}$. Besides, the catalyst stability in short time duration (1 hour) seems to increase with increasing temperature which may due to the increase of the degree of crystallinity of IrRu bimetallic catalyst. [56]

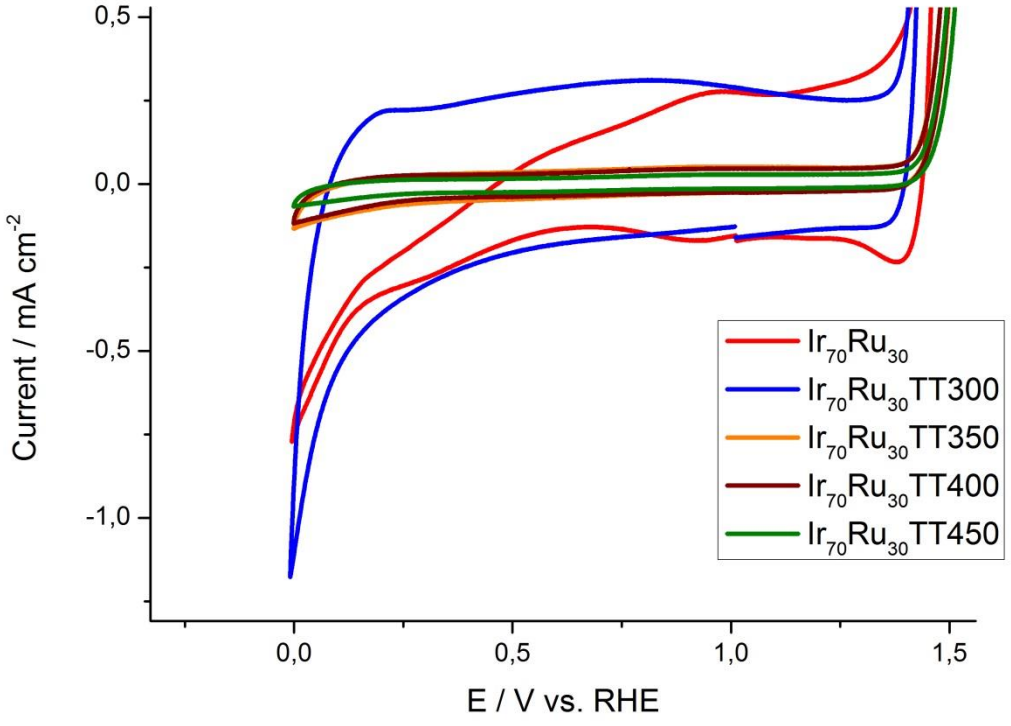

Figure 4-22 Cyclic voltammogram (iR-corrected) of different thermal treatment (300°C, 350°C, 400°C, 450°C) and as prepared $Ir_{70}Ru_{30}$ catalysts. Experiment duration: approximately 1 hour.

Figure 4-22 shows the cyclic voltammograms obtained at 20mV s^{-1} on sample with and without different annealing temperature. The very distinct and sharp anodic peaks for $Ir_{70}Ru_{30}$ and $Ir_{70}Ru_{30}$TT300 are associated with hydrogen adsorption on metallic iridium. Also, the hydrogen adsorption peak for $Ir_{70}Ru_{30}$TT300 is higher than as prepared $Ir_{70}Ru_{30}$ indicating an increase of active surface area after annealing at 300°C for half hour. These hydrogen adsorption peaks tends to disappear with annealing temperature larger than 350°C since

surface iridium will be irreversibly oxidized under such temperature as described in section 3.2.6. The anodic and cathodic current attributed to Ir (III) oxide to Ir (IV) oxide transition between 0.8 V to 1.2 V vs. RHE disappears when annealing temperature larger than 350°C indicating the irreversible oxidation for iridium at such temperature.

5 Conclusions

A series of supported iridium catalysts and unsupported bimetallic IrRu catalysts were synthesized using wet chemical synthesis method. Their activity and stability were investigated by using CV, chronopotentiometry and chronoamperometry. In addition, copper under potential deposition (Cu-UPD) on supported iridium catalyst was performed to determine the number of surface iridium atoms available for electrochemical reaction.

For supported catalysts, IrV/ATO shows the best OER activity with the lowest Tafel slope, 44 mV dec^{-1}, and highest mass-normalized current density, 115 A g^{-1}, at defined potential (1.51V vs. RHE) among all supported catalysts and Ir-nano benchmark catalyst. These excellent mass-normalized activity of the supported iridium catalysts may due to i) high iridium utilization since Ir nano-particles were well dispersed on the substrate materials ii) improved mass transportation, either water transportation or oxygen bubbles detachment, on the porous aerogel substrate surface.

Besides, the stability test and much harsher duty cycle test show that IrV/ATO has better stability compared to another two investigated catalysts, Ir/ATO and Ir-nano. During 15 hours stability test (at 1 mA cm^{-2}), the electrode potential increased dramatically after 5 and 12 hours for Ir-nano and Ir/ATO, respectively, indicating severe performance degradation with a loss of the active iridium particles. On the contrary, the potential of IrV/ATO was almost constant during the 15 hours stability test, evidencing a superior stability compared to Ir-nano and Ir/ATO. During the duty cycle test, Ir/ATO and Ir-nano catalysts were irreversibly degradated after 4th and 8th duty cycle, respectively. Again, the most stable catalyst was the IrV/ATO, which showed improved stability compared with another two catalysts in the duty cycle test. Even after 15 duty cycles, the potential at 1mA cm^{-2} increased only 0.28 V comparing that of first duty cycle.

From the Cu UPD test, we observed that Ir-nano benchmark catalyst showed the highest Cu UPD Stripping charge, which is not surprising since Ir-nano has the highest iridium loading

on the electrode. Among the four supported catalysts, IrV/ATO outperformed the other three supported catalysts with the largest amount of electrochemical surface sites, which is 12.4×10^{15} cm^{-2}.

Concerning unsupported bimetallic IrRu catalyst, as-prepared $Ir_{70}Ru_{30}$ and $Ir_{70}Ru_{30}$TT300 express much higher OER mass activity at 1.48 V vs. RHE ($\eta = 250mV$) compared with the other thermally treated catalysts. Besides, $Ir_{70}Ru_{30}$TT300 has an improved OER mass activity and also short time stability in comparison with as prepared $Ir_{70}Ru_{30}$.

In summary, the supported catalysts demonstrate better iridium usage with respect to active surface area, especially IrV/ATO catalyst. By introducing vanadium to the ATO supported iridium catalyst, the OER activity and stability were increased may due to better iridium distribution on the substrate and improving mass transportation in the aerogel substrate material. Cu UPD experiment also proved the increasing electrochemical surface active sites of IrV/ATO catalyst. Thus, we managed to develop the IrV/ATO as a feasible nanostructured oxygen electrocatalyst for PEM electrolyzer.

For better understanding, further investigations, such as EXAFS, TEM and AFM, are needed to find out the underlying mechanism for OER and what actually leads to the increases of OER activity and stability for IrV/ATO and $Ir_{70}Ru_{30}$TT300.

6 Bibliography

1. NEJATVEZIROGLU T. Hydrogen technology for energy needs of human settlements☆. *Int J Hydrogen Energy*. 1987;12(2):99-129. doi:10.1016/0360-3199(87)90086-3.

2. Muradov NZ, Veziroğlu TN. "Green" path from fossil-based to hydrogen economy: An overview of carbon-neutral technologies. *Int J Hydrogen Energy*. 2008;33(23):6804-6839. doi:10.1016/j.ijhydene.2008.08.054.

3. Carmo M, Fritz DL, Mergel J, Stolten D. A comprehensive review on PEM water electrolysis. *Int J Hydrogen Energy*. 2013;38(12):4901-4934. doi:10.1016/j.ijhydene.2013.01.151.

4. Eichman J, Harrison KW, Peters M. *Novel Electrolyzer Applications: Providing More than Just Hydrogen*. National Renewable Energy Laboratory; 2014.

5. Naterer GF, Fowler M, Cotton J, Gabriel K. Synergistic roles of off-peak electrolysis and thermochemical production of hydrogen from nuclear energy in Canada. *Int J Hydrogen Energy*. 2008;33(23):6849-6857.

6. Hedegaard K, Meibom P. Wind power impacts and electricity storage - A time scale perspective. *Renew Energy*. 2012;37(1):318-324. doi:10.1016/j.renene.2011.06.034.

7. Lettenmeier P, Wang L, Golla-Schindler U, et al. Nanosized IrOx-Ir Catalyst with Relevant Activity for Anodes of Proton Exchange Membrane Electrolysis Produced by a Cost-Effective Procedure. *Angew Chemie - Int Ed*. 2016;55(2):742-746. doi:10.1002/anie.201507626.

8. Haxel GB, Hedrick JB, Orris GJ, Stauffer PH, Hendley II JW. *Rare Earth Elements: Critical Resources for High Technology*.; 2002.

9. Vesborg PCK, Jaramillo TF. Addressing the terawatt challenge: scalability in the supply of chemical elements for renewable energy. *RSC Adv*. 2012;2(21):7933-7947.

10. Paoli EA, Masini F, Frydendal R, et al. Oxygen evolution on well-characterized mass-selected Ru and RuO 2 nanoparticles. *Chem Sci*. 2015;6(1):190-196.

11. Oh H-S, Nong HN, Reier T, Gliech M, Strasser P. Oxide-supported Ir nanodendrites with high activity and durability for the oxygen evolution reaction in acid PEM water electrolyzers. *Chem Sci*. 2015;6(6):3321-3328.

12. Nong HN, Oh HS, Reier T, et al. Oxide-supported IrNiOx core-shell particles as efficient, cost-effective, and stable catalysts for electrochemical water splitting. *Angew Chemie - Int Ed*. 2015;54(10):2975-2979. doi:10.1002/anie.201411072.

13. Zoulias E, Varkaraki E, Lymberopoulos N, Christodoulou CN, Karagiorgis GN. A review on water electrolysis. *TCJST*. 2004;4(2):41-71.

14. Jung H-Y, Huang S-Y, Ganesan P, Popov BN. Performance of gold-coated titanium bipolar plates in unitized regenerative fuel cell operation. *J Power Sources*. 2009;194(2):972-975.

15. Harrison KW, Remick R., Martin GD, Hoskin A. Hydrogen Production: Fundamentals and Case Study Summaries. *Hydrog fuel cells*. 2010;(January):207-226. doi:NREL/CP-550-47302.

16. Millet P, Mbemba N, Grigoriev SA, Fateev VN, Aukauloo A, Eti??vant C. Electrochemical performances of PEM water electrolysis cells and perspectives. *Int J Hydrogen Energy*. 2011;36(6):4134-4142. doi:10.1016/j.ijhydene.2010.06.105.

17. Larminie J, Dicks A, McDonald MS. *Fuel Cell Systems Explained*. Vol 2. J. Wiley Chichester, UK; 2003.

18. Bladergroen B, Su H, Pasupathi S, Linkov V. *Overview of Membrane Electrode Assembly Preparation Methods for Solid Polymer Electrolyte Electrolyzer*. INTECH Open Access Publisher; 2012.

19. Fabbri E, Habereder A, Waltar K, et al. Developments and perspectives of oxide-based catalysts for the oxygen evolution reaction. *Catal Sci Technol*. 2014;4(11):3800-3821. doi:10.1039/C4CY00669K.

20. Trasatti S. Electrocatalysis in the anodic evolution of oxygen and chlorine. *Electrochim Acta*. 1984;29(11):1503-1512. doi:10.1016/0013-4686(84)85004-5.

21. Park S, Shao Y, Liu J, Wang Y. Oxygen electrocatalysts for water electrolyzers and reversible fuel cells: status and perspective. *Energy Environ Sci*. 2012;5(11):9331-9344.

22. Rothenberg G. *Catalysis: Concepts and Green Applications*. John Wiley & Sons; 2015.

23. Park S, Shao Y, Liu J, Wang Y. Oxygen electrocatalysts for water electrolyzers and reversible fuel cells: status and perspective. *Energy Environ Sci*. 2012;5:9331. doi:10.1039/c2ee22554a.

24. Zeng K, Zhang D. Recent progress in alkaline water electrolysis for hydrogen production and applications. *Prog Energy Combust Sci*. 2010;36(3):307-326.

25. Wu J, Yuan XZ, Martin JJ, et al. A review of PEM fuel cell durability: degradation mechanisms and mitigation strategies. *J Power Sources*. 2008;184(1):104-119.

26. Millet P, Ngameni R, Grigoriev SA, et al. PEM water electrolyzers: from electrocatalysis to stack development. *Int J Hydrogen Energy*. 2010;35(10):5043-5052.

27. Kötz R, Neff H, Stucki S. Anodic Iridium Oxide Films XPS-Studies of Oxidation State Changes and. *J Electrochem Soc*. 1984;131(1):72-77.

28. Hepel T, Pollak FH, O'Grady WE. Irreversible Voltammetric Behavior of the (100) IrO2 Single-Crystal Electrodes in Sulfuric Acid Medium. *J Electrochem Soc*. 1985;132(10):2385-2390.

29. Kötz R, Stucki S. Stabilization of RuO 2 by IrO 2 for anodic oxygen evolution in acid media. *Electrochim Acta*. 1986;31(10):1311-1316.

30. Kötz R, Lewerenz HJ, Stucki S. XPS studies of oxygen evolution on Ru and RuO2 anodes. *J Electrochem Soc*. 1983;130(4):825-829.

31. Rogers DB, Shannon RD, Sleight AW, Gillson JL. Crystal chemistry of metal dioxides with rutile-related structures. *Inorg Chem*. 1969;8(4):841-849.

32. Yeo RS, Orehotsky J, Visscher W, Srinivasan S. Ruthenium-Based Mixed Oxides as Electrocatalysts for Oxygen Evolution in Acid Electrolytes. *J Electrochem Soc*. 1981;128(9):1900-1904.

33. Miles MH, Thomason MA. Periodic variations of overvoltages for water electrolysis in acid solutions from cyclic voltammetric studies. *J Electrochem Soc*. 1976;123(10):1459-1461.

34. Ozouf G, Beauger C. Niobium-and antimony-doped tin dioxide aerogels as new catalyst supports for PEM fuel cells. *J Mater Sci*. 2016;51(11):5305-5320.

35. Matsumoto Y, Sato E. Electrocatalytic properties of transition metal oxides for oxygen evolution reaction. *Mater Chem Phys*. 1986;14(5):397-426.

36. Chakrapani K, Sampath S. The dual role of borohydride depending on reaction temperature: synthesis of iridium and iridium oxide. *Chem Commun*. 2015;51(47):9690-9693.

37. Islam A, Anwarul Kabir Bhuiya M, Saidul Islam M. A Review on Chemical Synthesis Process of Platinum Nanoparticles. *Asia Pacific J Energy Environ*. 2014;1(2):107. doi:10.15590/apjee/2014/v1i2/53749.

38. Barsoukov E, Macdonald JR. *Impedance Spectroscopy: Theory, Experiment, and Applications*. John Wiley & Sons; 2005.

39. Randles JEB. Kinetics of rapid electrode reactions. *Discuss faraday Soc*. 1947;1:11-19.

40. Burke LD, Lyons ME, Murphy OJ. Formation of hydrous oxide films on cobalt under potential cycling conditions. *J Electroanal Chem Interfacial Electrochem*. 1982;132:247-261.

41. Hackwood S, Schiavone LM, Dautremont-Smith WC, Beni G. Anodic evolution of oxygen on sputtered iridium oxide films. *J Electrochem Soc*. 1981;128(12):2569-2573.

42. Nong HN, Oh H, Reier T, et al. Oxide-Supported IrNiOx Core–Shell Particles as Efficient, Cost-Effective, and Stable Catalysts for Electrochemical Water Splitting. *Angew Chemie Int Ed*. 2015;54(10):2975-2979.

43. Hachiya T, Honbo H, Itaya K. Detailed underpotential deposition of copper on gold (III) in aqueous solutions. *J Electroanal Chem interfacial Electrochem*. 1991;315(1-2):275-291.

44. Markovic N, Ross PN. Effect of anions on the underpotential deposition of copper on platinum (111) and platinum (100) surfaces. *Langmuir*. 1993;9(2):580-590.

45. Green CL, Kucernak A. Determination of the platinum and ruthenium surface areas in platinum-ruthenium alloy electrocatalysts by underpotential deposition of copper. I. Unsupported catalysts. *J Phys Chem B*. 2002;106(5):1036-1047.

46. Chyan OMR. Electrochemical Study of Under-potential Deposition Processes on Transition Metal Surfaces. 2006.

47. Arikawa T, Takasu Y, Murakami Y, Asakura K, Iwasawa Y. Characterization of the structure of RuO2-IrO2/Ti electrodes by EXAFS. *J Phys Chem B*. 1998;102(19):3736-3741.

48. Tran V-H, Yatabe T, Matsumoto T, et al. An IrSi oxide film as a highly active water-oxidation catalyst in acidic media. *Chem Commun*. 2015;51(63):12589-12592.

49. Ouattara L, Fierro S, Frey O, Koudelka M, Comninellis C. Electrochemical comparison of IrO2 prepared by anodic oxidation of pure iridium and IrO2 prepared by thermal decomposition of H2IrCl6 precursor solution. *J Appl Electrochem*. 2009;39(8):1361-1367.

50. Watt J, Cheong S, Toney MF, et al. Ultrafast growth of highly branched palladium nanostructures for catalysis. *ACS Nano*. 2009;4(1):396-402.

51. Lim B, Jiang M, Camargo PHC, et al. Pd-Pt Bimetallic Nanodendrites with.

52. Wen T, Hu C. Hydrogen and Oxygen Evolutions on Ru-Ir Binary Oxides. *J Electrochem Soc*. 1992;139(8):2158-2163.

53. Juodkazytė J, Šebeka B, Valsiunas I, Juodkazis K. Iridium anodic oxidation to Ir (III) and Ir (IV) hydrous oxides. *Electroanalysis*. 2005;17(11):947-952.

54. Kolb DM, Przasnyski M, Gerischer H. Underpotential deposition of metals and work function differences. *J Electroanal Chem Interfacial Electrochem*. 1974;54(1):25-38.

55. Ma H, Liu C, Liao J, Su Y, Xue X, Xing W. Study of ruthenium oxide catalyst for electrocatalytic performance in oxygen evolution. *J Mol Catal A Chem*. 2006;247(1):7-13.

56. Rasten E, Hagen G, Tunold R. Electrocatalysis in water electrolysis with solid polymer electrolyte. *Electrochim Acta*. 2003;48(25):3945-3952.

7 Appendix

A Appendix: EDX

The datas of Ir/NTO and Ir/ATO$_{H2O2}$ obtained by EDX analysis are given below in wt%.

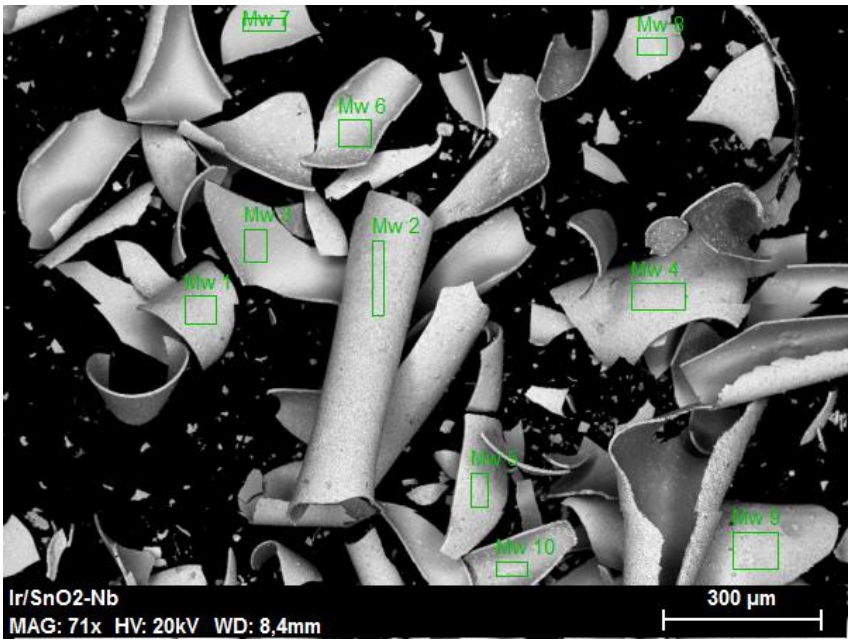

Table 12 Elemental analysis of Ir/ATO catalyst

Spectrum	C	O	Na	Nb	Sn	Ir
wt %						
Mw 1	8.4	11.56	0.84	1.78	27.52	49.9
Mw 2	7.17	13.29	0.82	2.65	36.39	39.67
Mw 3	5.5	13.27	0.97	5.01	54.86	20.4
Mw 4	6.9	9.18	0.72	2.78	36.31	44.1
Mw 5	5.49	8.51	0.13	2.54	33.55	49.78
Mw 6	4.89	6.31	0.69	3.05	47.14	37.92
Mw 7	72.83	19.83	0.1	0.22	3.92	3.11
Mw 8	71.91	18.19	0	0.35	5.48	4.07
Mw 9	6.11	8.84	0	2.8	48.21	34.04
Mw 10	3.71	5.43	0.32	2.26	34.77	53.51
Average	19.291	11.441	0.459	2.344	32.815	33.65
Standard deviation	28.01	4.78	0.39	1.37	16.89	18.46

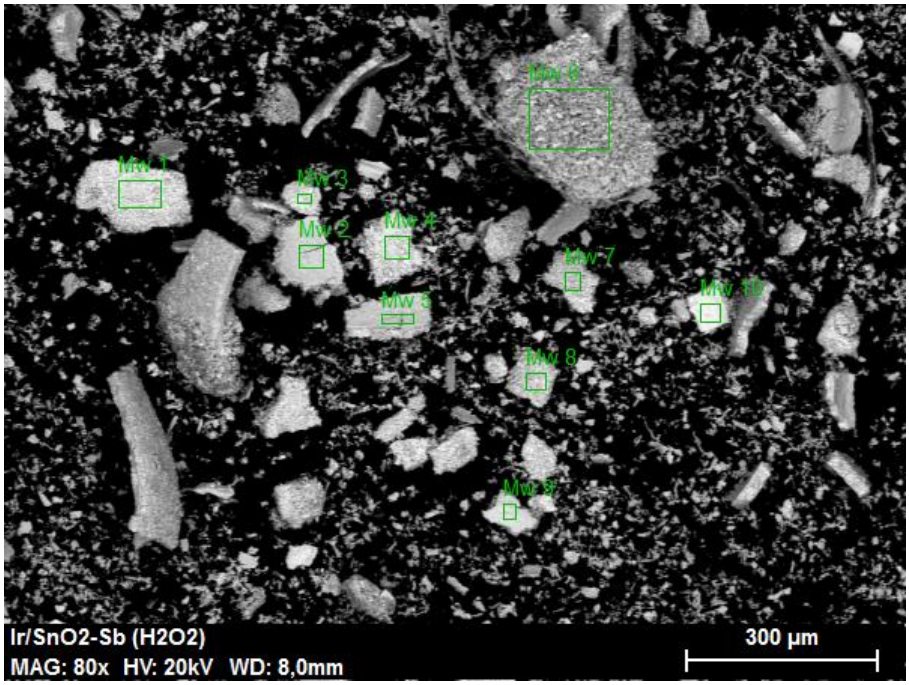

Table 13 Elemental analysis of Ir/ATO catalyst

Spectrum	C	O	Na	Cl	Sn	Sb	Ir
wt %							
Mw 1	4.67	8.39	1.39	2.3	35.79	14.94	32.53
Mw 2	6.46	17.02	1.61	2.27	34.05	12.91	25.68
Mw 3	7.41	13.07	1.15	2.46	28.91	11.36	35.63
Mw 4	5.77	12.36	0.98	1.85	38.02	14.59	26.43
Mw 5	8.09	19.38	1.15	1.74	32.84	12	24.8
Mw 6	9.26	19.89	2.04	1.44	41.62	5.48	20.27
Mw 7	5.48	12.49	1.18	2.16	44	5.88	28.8
Mw 8	4.33	8.78	1.41	2.95	40.42	16.67	25.45
Mw 9	4.82	8.62	0.98	4.08	33.8	13.92	33.77
Average	6.25	13.33	1.32	2.36	36.61	11.97	28.15
Standard deviation	1.69	4.50	0.34	0.78	4.81	3.91	4.96

B Appendix: SEM

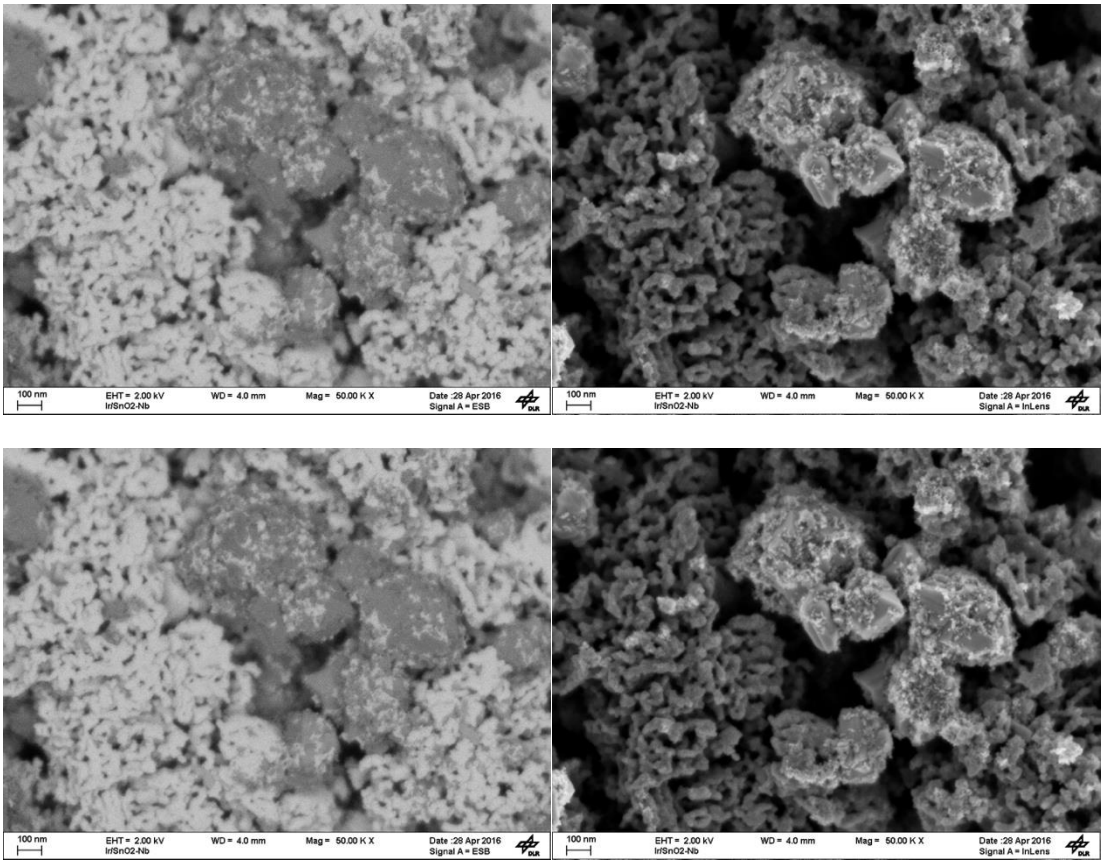

SEM images of Ir/NTO catalyst, Low (upper) and High (lower) magnification SEM iamges of Ir/ATO catalyst. Left side image acquired with Secondary electron sensor and the right side image acquired from back-scattered electron detector.

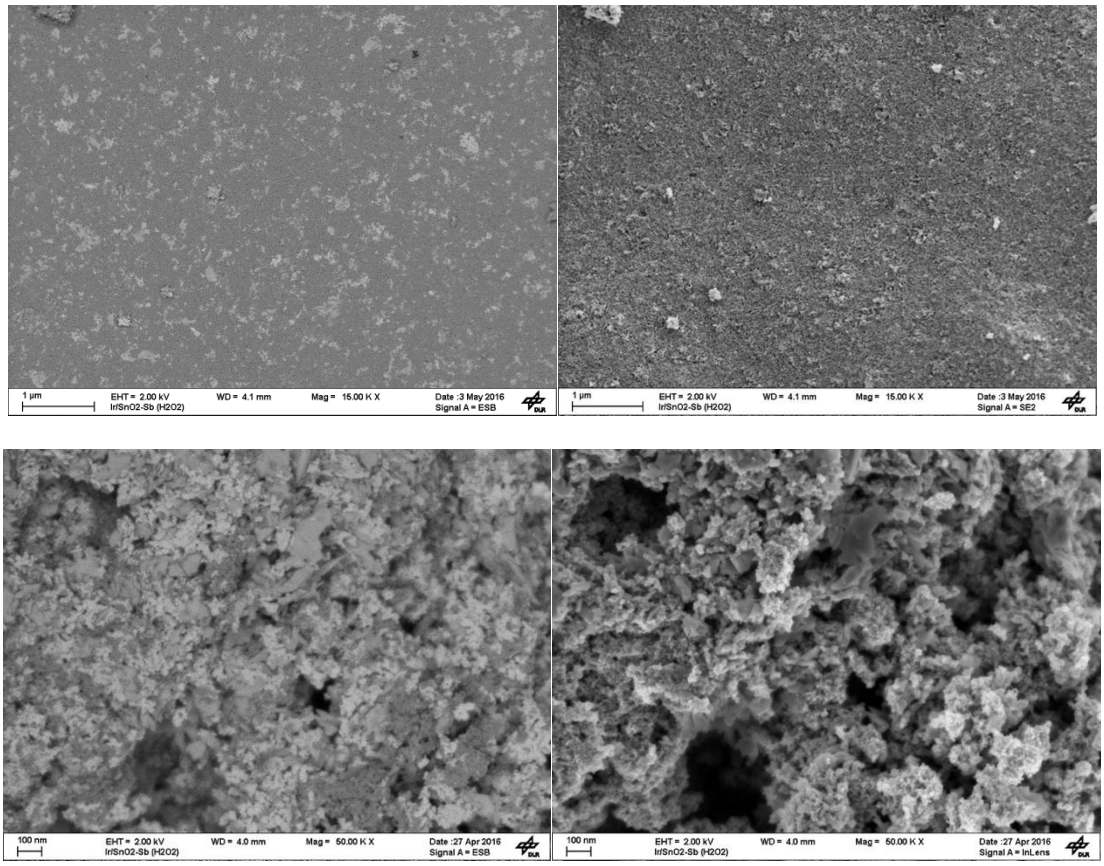

SEM images of Ir/NTO catalyst, Low (upper) and High (lower) magnification SEM iamges of Ir/ATO catalyst. Left side image acquired with Secondary electron sensor and the right side image acquired from back-scattered electron detector.